A lipocalin mediates unidirectional haem biomineralization in malaria parasites

Joachim M. Matz[1,2,*], Benjamin Drepper[2], Thorsten B. Blum[3], Eric van Genderen[3], Alana Burrell[4], Peer Martin[2], Thomas Stach[2], Lucy Collinson[4], Jan Pieter Abrahams[3,5,6], Kai Matuschewski[2] & Michael J. Blackman[1,7]

[1] Malaria Biochemistry Laboratory, The Francis Crick Institute, London, UK
[2] Department of Molecular Parasitology, Institute of Biology, Humboldt University, Berlin, Germany
[3] Laboratory of Nanoscale Biology, Division of Biology and Chemistry, Paul Scherrer Institute, Villigen, Switzerland
[4] Electron Microscopy Science Technology Platform, The Francis Crick Institute, London, UK
[5] Center for Cellular Imaging and NanoAnalytics, Biozentrum, University of Basel, Basel, Switzerland.
[6] Institute of Biology, Leiden University, Leiden, The Netherlands.
[7] Faculty of Infectious and Tropical Diseases, London School of Hygiene & Tropical Medicine, London, UK
* Corresponding and lead author: J.M.M., joachim.matz@crick.ac.uk, https://orcid.org/0000-0002-0575-0412

ABSTRACT

During blood stage development, malaria parasites are challenged with the detoxification of enormous amounts of haem released during the proteolytic catabolism of erythrocytic haemoglobin. They tackle this problem by sequestering haem into bioinert crystals known as haemozoin. The mechanisms underlying this biomineralization process remain enigmatic. Here, we demonstrate that both rodent and human malaria parasite species secrete and internalize a lipocalin-like protein, PV5, to control haem crystallization. Transcriptional deregulation of *PV5* in the rodent parasite *Plasmodium berghei* results in inordinate elongation of haemozoin crystals, while conditional *PV5* inactivation in the human malaria agent *Plasmodium falciparum* causes excessive multi-directional crystal branching. Although haemoglobin processing remains unaffected, PV5-deficient parasites generate less haemozoin. Electron diffraction analysis indicates that despite the distinct changes in crystal morphology neither the crystalline order nor unit cell of haemozoin are affected by impaired PV5 function. Deregulation of *PV5* expression renders *P. berghei* hypersensitive to the antimalarial drugs artesunate, chloroquine, and atovaquone, resulting in accelerated parasite clearance following drug treatment *in vivo*. Together, our findings demonstrate the *Plasmodium*-tailored role of a lipocalin family member in haemozoin formation and underscore the haem biomineralization pathway as an attractive target for therapeutic exploitation.

KEYWORDS *Plasmodium*, malaria, hemozoin, haem, heme, haemozoin, vacuole, lipocalin

SIGNIFICANCE

During blood stage development, the malaria parasite replicates inside erythrocytes of the vertebrate host, where it engulfs and digests most of the available haemoglobin. This results in release of the oxygen-binding prosthetic group haem, which is highly toxic in its unbound form. The parasite crystallizes the haem into an insoluble pigment called haemozoin, a process that is vital for parasite survival and which is exploited in antimalarial therapy. We demonstrate that the parasite uses a protein called PV5 in haemozoin formation and that interfering with PV5 expression can increase the parasite's sensitivity to antimalarial drugs during blood infection. An improved understanding of the mechanisms underlying haem sequestration will provide valuable insights for future drug development efforts.

47 **INTRODUCTION**

48 The devastating pathology of malaria is caused by infection of red blood cells with unicellular
49 *Plasmodium* parasites which reside within an intraerythrocytic parasitophorous vacuole (PV)
50 (1). Throughout blood stage development, the parasite ingests and catabolizes up to 80% of
51 the host cell cytoplasm, facilitating amino acid acquisition and making sufficient room for
52 parasite growth (2, 3). Haemoglobin is incorporated through endocytosis and then degraded
53 by an array of functionally redundant proteases, a process which occurs in acidified lysosome-
54 like organelles with species-specific morphology (4). In the rodent-infective parasite species
55 *Plasmodium berghei*, one or more food vacuoles (FVs) give rise to small digestive vesicles
56 (DVs) which only fuse at the very end of intraerythrocytic development (5). By contrast, the
57 most virulent agent of human malaria, *Plasmodium falciparum*, directs all endosomal traffic to
58 a single large FV, where proteolysis occurs (6).

59 Here, haemoglobin digestion is accompanied by the release of high levels of the
60 porphyrin co-factor haem from the globin chains. Haem can damage proteins and lipids
61 through various mechanisms, including the formation of free radicals (7). The unique
62 challenge of haem detoxification is met by the parasite's capacity to sequester the released
63 haem into a bioinert crystalline product called haemozoin (Hz), which accumulates in the FV
64 or DVs. Haem is initially oxidised to yield haematin, which then dimerizes through the
65 reciprocal coordination of iron and propionate moieties. This molecular unit then assembles
66 into Hz crystals which typically take the form of triclinic high aspect ratio parallelograms (8-
67 10). By the end of intraerythrocytic development, all the Hz crystals are contained within a
68 central residual body, which is eventually released upon parasite egress from the host cell
69 and which contributes to the inflammatory responses associated with acute malaria (11). The
70 mechanism of Hz formation is highly debated. While several studies suggest a
71 physicochemical and autocatalytic crystallization process (12-15), there have been reports of
72 parasite proteins (16-18) and lipids (19-21) promoting Hz assembly *in vitro*.

73 The parasite's dependency on haem detoxification has long been exploited in
74 antimalarial therapy with outstanding success. Aminoquinolines inhibit Hz formation *via* direct
75 physical interactions with haematin and the crystal surface, eventually leading to the build-up
76 of cytotoxic free haem (22-25). The aminoquinoline chloroquine was the front-line medication
77 against malaria from the 1950s onward until the emergence of wide-spread drug resistance
78 restricted its utility (26). Nonetheless, to this day, chloroquine remains among the most
79 effective antimalarial drugs ever developed, highlighting the outstanding importance of haem

80 sequestration for *Plasmodium* survival. It is thus crucial for future drug development efforts to
81 gain a better understanding of the mechanisms underlying this unique biomineralization event.

82 In this report, we demonstrate that a parasite-encoded lipocalin called PV5 is a central
83 regulator of *Hz* formation.

84 **RESULTS**

85 **Malaria parasites encode a lipocalin-like protein, PV5**

86 Employing a genome-wide *in silico* down-scaling approach, we previously identified an
87 essential *P. berghei* PV protein, *Pb*PV5 (PBANKA_0826700), which has orthologues in all
88 other *Plasmodium* species, including *P. falciparum* (PF3D7_0925900) (27). Inspection of the
89 PV5 amino acid sequence revealed a striking similarity to members of the functionally diverse
90 lipocalin family, barrel-shaped proteins capable of binding various hydrophobic ligands and/or
91 protein interaction partners (28). The signature lipocalin fold comprises a short amino-terminal
92 helix followed by eight consecutive barrel-forming β-strands, another α-helix and one more β-
93 strand (Fig. 1*A*) (29). In addition, PV5 harbours two preceding amino-terminal β-strands
94 specific to *Plasmodium*, as well as a signal peptide. Multiple sequence alignments with
95 lipocalins from phylogenetically distant organisms showed the presence of a highly conserved
96 glycine and two aromatic amino acids within the structurally conserved region 1 (SCR1) of
97 PV5, a hallmark of the extended calycin superfamily (Fig. 1*A*) (29). Among several structural
98 homologues, the bacterial outer membrane lipocalin Blc from *Escherichia coli* was predicted
99 to share the highest similarity with PV5. Homology modelling guided by the known *E. coli* Blc
100 structure suggests that PV5 shares the overall architecture of the lipocalin family including the
101 characteristic β-barrel (Fig. 1*B*). Together, the sequence signatures and predicted structural
102 features support membership of *Plasmodium* PV5 in the calycin protein superfamily.

103 **PV5 is trafficked to the parasite's digestive compartments**

104 We first investigated the spatiotemporal expression of *Pb*PV5 during asexual blood stage
105 development. Live fluorescence microscopy of transgenic *P. berghei* parasites expressing
106 mCherry-3xMyc-tagged *Pb*PV5 confirmed that the protein localizes to tubular PV extensions
107 during ring and trophozoite stages and surrounds individual merozoites in segmented
108 schizonts (Fig. 1*C*) (27). In addition, a substantial fraction of the protein was restricted to the
109 parasite cytoplasm. This was particularly prominent in schizonts, where intraparasitic *Pb*PV5
110 appeared to localize to the Hz-containing residual body (Fig. 1*C*). In merozoites, mCherry
111 fluorescence was concentrated in a punctate intraparasitic region, perhaps signifying storage
112 of *Pb*PV5 in the dense granules, as has been demonstrated for several other important PV
113 proteins (30-32), but this fraction was minimal as compared to the protein contained in the
114 residual body. Quantification of the mCherry-fluorescence intensity in live parasites indicated
115 that *Pb*PV5 is much more abundant in mature parasite stages than in rings and merozoites,
116 suggesting substantial levels of *de novo* synthesis throughout parasite maturation (Fig 1*C*).

117 In trophozoites, the intraparasitic fraction of *Pb*PV5 was associated with spherical
118 structures at the parasite periphery (Fig. 1*C*) and microscopic examination of mechanically
119 expanded free parasites revealed that these were the Hz-containing DVs (Fig. 1*D)*. To test
120 whether this localization is conserved across different *Plasmodium* species, we generated
121 similar transgenic *P. falciparum* parasites expressing mCherry-tagged *Pf*PV5. Here, a small
122 fraction of the fusion protein consistently localized to the PV, whereas the majority of the
123 fluorescent signal overlapped with the Hz crystals and with the signal of the acidotropic dye
124 Lysosensor Blue DND-167, which accumulates in the acidic FV (Fig. 1*E*). In addition, we
125 frequently observed smaller *Pf*PV5-positive foci in the parasite cytoplasm, most likely
126 reflecting early endosomal compartments (Fig. 1*E*). Subcellular fractionation of tagged *P.*
127 *berghei* parasites revealed that *Pb*PV5 is freely soluble (Fig. 1*F*). These finding are in good
128 agreement with the detection of *Pf*PV5 in the FV proteome of *P. falciparum* (33). Together,
129 our observations suggest that in both *Plasmodium* species PV5 is first secreted into the PV
130 and then internalized through endocytosis of host cell cytoplasm to accumulate in the matrix
131 of the parasite's digestive compartments.

132 **Transcriptional deregulation of Pb*PV5* impairs asexual parasite propagation *in vivo***

133 Our previous attempts to disrupt the genomic Pb*PV5* locus resulted only in atypical integration
134 of the targeting construct without perturbing the endogenous gene, which is indicative of
135 essential functions during the asexual blood stage cycle *in vivo* (27). As an alternative genetic
136 strategy to analyse Pb*PV5* function, we sought to deregulate Pb*PV5* expression by employing
137 a promoter swap approach (Fig. 2*A*). Towards this aim, we generated parasites expressing
138 the endogenous Pb*PV5* gene from the promoters of *Plasmodium* translocon of exported
139 proteins 88 (*PTEX88*) or heat shock protein 101 (*HSP101*), respectively (Fig. S1 *A* and *B*).
140 Quantitative real-time PCR analysis of the mutants indicated that the knock-down efficiency
141 was ~60% in asynchronous blood stages (Fig. S1*C*). Impaired growth prevented quantification
142 of knock-down levels in synchronized *ex vivo* early blood stages. Strikingly, in the schizont
143 stage, mutants exhibited significantly elevated Pb*PV5* transcript levels, corresponding to ~3.4
144 (*pv5::5'ptex88*) and ~5.6 times (*pv5::5'hsp101*) more than in WT schizonts (Fig. S1*C*).
145 Therefore, using the promoter swap strategy, we succeeded in deregulating the physiological
146 expression of Pb*PV5* throughout the asexual replication cycle.

147 To investigate whether altered Pb*PV5* transcription results in reduced parasite fitness,
148 we examined asexual propagation of the mutants *in vivo*. Growth of the promoter swap
149 mutants was significantly impaired, with the *pv5::5'ptex88* parasites growing at 80% and
150 *pv5::5'hsp101* parasites at only 54% of the WT growth rate (Fig. 2*B*). These results underline
151 the importance of correct Pb*PV5* expression during asexual replication of the parasite *in vivo*.

152 **Pb*PV5* mutants form less haemozoin**

153 Inspection of Giemsa-stained thin blood films revealed striking morphological differences
154 between WT parasites and the promoter swap mutants. During the trophozoite stage, the FV
155 of the mutants was significantly swollen, visible as a large translucent area within the parasite
156 cytoplasm close to the nucleus (Fig. 2*C*). Microscopic quantification revealed this area to be
157 1.5-fold (*pv5::5'ptex88*) or 1.8-fold (*pv5::5'hsp101*) larger than in WT parasites (Fig. S2*A*).
158 Vacuolar swelling was transient, as mature schizonts did not exhibit comparable abnormalities
159 (Fig. 2*C*).

160 Another striking phenomenon was the low visibility of dark granular material in mutant
161 trophozoites, when compared to WT (Fig. 2*C*). This lack of granularity was most noticeable in
162 the *pv5::5'hsp101* mutant and became particularly apparent during the gametocyte stage,
163 where pigment granules are usually very prominent. To validate this finding, we subjected
164 mixed blood stage parasites to flow cytometry and measured the intensity of the side scattered
165 light, a commonly used proxy for cellular granularity (Fig. 2*D*). In agreement with our
166 microscopic analysis, the Pb*PV5* mutants displayed reduced side scattering and the
167 phenotype was again more severe in the *pv5::5'hsp101* mutant.

168 Because we suspected a Hz formation defect in the mutants, we fixed intraerythrocytic
169 parasites with methanol and subjected them to polarization microscopy, which exploits the
170 birefringent properties of Hz to specifically visualize the crystals. Using this method, we
171 detected a weaker signal for the mutants, which correlated with reduced visibility of dark
172 pigment in brightfield (Fig. 2*E*). Enumeration of individual bright entities suggested the
173 presence of fewer Hz-containing structures within the mutants (~80% of WT) (Fig. 2*E*).
174 Quantification of the polarized light intensity also indicated that *pv5::5'ptex88* parasites form
175 only 64% and the *pv5::5'hsp101* 61% of the Hz generated in WT parasites (Fig. 2*F*). Together,
176 these observations show that perturbation of Pb*PV5* expression results in reduced haem
177 biomineralization *in vivo*.

178 **Protracted haemozoin extension upon deregulation of Pb*PV5* expression**

179 We next aimed to examine how lower levels of Hz correlate with crystal size. To do this, we
180 isolated Hz from mixed blood stage parasites and examined the material by scanning electron
181 microscopy (SEM). This confirmed the characteristic high aspect ratio parallelogram
182 morphology of WT Hz (Fig. 3 *A* and *B*). Strikingly, this was not the case for crystals isolated
183 from the promoter swap mutants. Hz from both transgenic parasite strains exhibited highly
184 irregular shapes and rough edges and showed only few of the distinctive Hz crystal vertices
185 (Fig. 3*B*). Crystals from *pv5::5'ptex88* parasites most often had a pointed and canine tooth-

186 like appearance, extending from a single straight crystal face. These abnormalities were even
187 more pronounced in the *pv5::5'hsp101* mutant, where in most cases there was a region of
188 normal crystal morphology with 2 or 3 straight edges, corresponding to the {010}, {011} and
189 {001} faces. From this regular parent crystal emerged an enormous outgrowth which usually
190 surpassed the dimensions of the parent crystal (Fig. 3*B*). This outgrowth consistently grew at
191 an obtuse angle of ~105° in relation to the dominant *c* axis of the parent crystal, although
192 accurate determination of the angle was complicated by the slightly bent and irregular shape
193 of the outgrowth, which might be attributed to the space restrictions encountered in the *P.*
194 *berghei* DVs. The outgrowth's angle was not reflected in the physiological morphology of Hz
195 (Fig. 3 *A* and *B*) and at least two faces of the regular parent crystal appeared to be involved.
196 Indeed, in most cases, the outgrowth emerged from sites where the {010} and {011} faces
197 meet and always grew along a plane corresponding to one of the original crystal faces (Fig.
198 3*B*). Other crystal formations were also observed, albeit at lower frequency, including some
199 with multiple crystal branches and some with very rough surfaces (Fig. S2*B*). We observed
200 similar crystal abnormalities *in situ* by transmission electron microscopy (TEM) of purified
201 schizonts (Fig. 3*C*).

202 Despite the lower overall levels of Hz formed and the abnormal crystal morphology,
203 we found that the mutants formed larger Hz crystals as indicated by the area exposed to the
204 SEM electron beam (Fig. 3*D*). The *pv5::5'hsp101* mutant formed the largest crystals, which
205 were ~180% of WT size, while the *pv5::5'ptex88* crystals were at 130%. Importantly, the
206 mutant Hz crystals displayed greater dimensions only in length but not in width owing to the
207 unidirectional expansion of the outgrowth (Fig. 3*D*). Examination of the parent crystals from
208 *pv5::5'hsp101* parasites showed that these were roughly half the size of whole WT crystals
209 (Fig. 3*D*). The aspect ratios of WT crystals and the *pv5::5'hsp101* parent crystals were
210 identical, together indicating that a period of normal crystallisation during earlier *pv5::5'hsp101*
211 parasite development is followed by irregular crystal extension later on (Fig. 3*E*). Inspection
212 of Hz from an unrelated slow-growing mutant (35) and from chloroquine-treated WT parasites
213 ruled out a secondary effect of reduced parasite fitness or mortality on Hz morphology (Fig.
214 S2 *C* and *D*).

215 To determine whether the crystalline order was affected by deregulation of Pb*PV5*, we
216 obtained electron diffraction patterns from WT- and *pv5::5'hsp101*-derived Hz (Fig. 3*F*) and
217 analysed the maximum diffracted intensities in concentric bins as a function of resolution.
218 There was no difference in the drop-off of diffracted intensity between WT and mutant and the
219 peak positions of the maxima corresponded (Fig. 3*G*). Differences in the magnitude of
220 individual peaks can be attributed to preferential orientation, especially of the *pv5::5'hsp101*-
221 derived crystals, which most often come to lie at their {100} faces. Together, these data

222 indicate no differences in crystalline order or unit cell upon functional impairment of Pb*PV5*
223 and we conclude that altered crystal morphology is not caused by alternative nucleation into
224 a different haematin polymorph. Thus, deregulation of Pb*PV5* leads to the formation of ordered
225 elongated Hz crystals with a highly variable and abnormal habit.

226 **Loss of PV5 causes haemozoin branching in *P. falciparum***

227 To investigate the consequences of *PV5* disruption, we generated a conditional *PV5* knockout
228 line of the human pathogen *P. falciparum*, allowing rapamycin-induced DiCre-mediated
229 excision of the Pf*PV5* gene (Fig. 4*A* and Fig. S3*A*). Correct modification of the locus was
230 indicated by diagnostic PCR and by the successful tagging of *Pf*PV5 with a 3xHA tag, as
231 demonstrated by Western blot and immunofluorescence analysis (Fig. 4 *B* and *C*, Fig. S3 *B*-
232 *D*). 3xHA-tagged *Pf*PV5 localized to the PV and to intraparasitic vesicular structures (Fig. S3*C*
233 and *D*). Surprisingly, no signal was observed within the central FV, in marked contrast to the
234 mCherry fusion protein (Fig. 1*E*) and despite previous evidence from FV proteomics (33). Most
235 likely, the 3xHA-tag is obscured or processed in the FV.

236 Treatment of *pv5-3xHA:loxP* parasites with rapamycin led to efficient gene excision
237 and complete loss of *Pf*PV5 protein expression during the same intraerythrocytic cycle (Fig. 4
238 *B* and *C*, Fig. S3*D*). This did not detectably affect parasite maturation but did result in a modest
239 merozoite invasion defect upon rupture of the Pf*PV5*-null schizonts, reducing parasite
240 replication (Fig. S4). Extended monitoring of the rapamycin-treated parasites indicated an
241 estimated fitness cost of ~40% (Fig. S4*B*). This is in good agreement with a proposed
242 mutagenesis index score of 0.22 from a genome-wide piggy-Bac insertion mutagenesis
243 screen (36). Accordingly, Pf*PV5,* although not essential under standard *P. falciparum* culture
244 conditions, is required for optimal parasite propagation *in vitro*.

245 To examine the effects of Pf*PV5* ablation on haem biomineralization, Hz was
246 visualized and quantified by polarization microscopy. Rapamycin-treated *pv5-3xHA:loxP*
247 parasites formed only 57% of the Hz observed in WT and DMSO-treated controls and
248 individual crystals appeared to be globular rather than elongated (Fig. 4 *D* and *E*). In the
249 absence of *Pf*PV5, Hz released at parasite egress no longer formed clusters of separate
250 slender crystals but rather appeared as aggregates which only occasionally fell apart into
251 individual globular units (Fig. 4*F*). In good agreement, microscopic inspection of live parasites
252 revealed that the characteristic twirling motion of Hz within the central FV was largely lost upon
253 Pf*PV5* knockout (Fig. 4*G* and Movie S1).

254 The dramatic abnormalities in *Hz* crystal morphology resulting from ablation of Pf*PV5*
255 were even more evident by SEM analysis. While WT parasites formed crystals of the expected

256 brick-like morphology, individual Hz units from rapamycin-treated *pv5-3xHA:loxP* parasites
257 appeared smaller and more globular (Fig. 4*H* and Table S1). The surfaces of these Hz units
258 were covered in scales and stubby crystal buds. Individual crystals of comparable bud-like
259 dimensions were not observed, indicating a branching rather than an aggregation
260 phenomenon. In some instances, a lower number of crystal buds allowed the visualization of
261 an ordered Hz core, suggesting that branching is initiated from a regular parent crystal (Fig.
262 4*H*). We detected several morphological intermediates between slightly scaled Hz, highly
263 branched crystal units and fused congregations (Fig. 4*H*). We frequently observed enormous
264 aggregates of spherical proportions, mirroring the shape of the central FV (Fig. 4*H*). This
265 suggested that hyperactive crystal branching in the absence of *Pf*PV5 caused individual
266 studded Hz units to stick together and subsequently merge during Hz growth, which might
267 explain the absence of motion in the parasite FV (Fig. 4*H*). Non-rapamycin-treated *pv5-*
268 *3xHA:loxP* control parasites mainly formed regular Hz crystals, however 27.5% of the crystals
269 exhibited a modest degree of branching (Fig. 4*H* and Table S1). Furthermore, crystal size and
270 aspect ratio were reduced in comparison to WT parasites, suggesting a moderate functional
271 impairment of 3xHA-tagged *Pf*PV5 (Fig. 4*H* and Table S1). Our data demonstrate that PV5 is
272 critical for the efficient sequestration of haem and for the ordered expansion of Hz crystals in
273 *P. falciparum*.

274 **Efficient haemoglobin processing in the absence of *Pf*PV5**

275 To exclude an indirect effect mediated by defective haemoglobin catabolism, we
276 examined the haemoglobin content of saponin-released parasites. *Pf*PV5-deficient ring stages
277 and trophozoites contained normal quantities of internalized haemoglobin (Fig. 5*A*). Only
278 mature segmented *pv5-3xHA:loxP* schizonts exhibited slightly elevated concentrations of
279 residual haemoglobin upon induction (Fig. 5*B*). However, this was also observed in WT
280 schizonts upon rapamycin treatment, suggesting a minor compound-specific effect.
281 Furthermore, saponin treatment released normal amounts of haemoglobin from schizont-
282 infected erythrocytes in the absence of *Pf*PV5, indicating unaltered haemoglobin ingestion
283 (Fig. 5*B*). As a positive control for perturbation of haemoglobin catabolism, we cultured WT
284 parasites in the presence of the protease inhibitor E64. Vacuolar bloating, as readily detected
285 by E64 treatment, was not visible in rapamycin-treated *pv5-3xHA:loxP* parasites (Fig. 5*C*). We
286 also note that, unlike Pf*PV5* deletion, E64 treatment produced no changes in the architecture
287 of Hz (Fig. 5*D*). In addition, *Pf*PV5-deficient parasites retained normal E64 sensitivity (Fig. 5
288 *E* and *F*). Combined, these findings suggest that inhibition of haemoglobin catabolism does
289 not directly translate into altered Hz morphology and that *Pf*PV5 is not involved in the overall
290 consumption of host cell cytoplasm.

291 **Pb*PV5* expression influences antimalarial drug sensitivity *in vivo***

292 In the light of our evidence implicating PV5 in Hz formation, we next tested whether parasites
293 with affected PV5 function display altered sensitivity towards chloroquine, a 4-aminoquinoline
294 which is thought to inhibit haem biomineralization in *Plasmodium* (22-25). The absence of
295 *Pf*PV5 did not detectably alter chloroquine sensitivity in cultured *P. falciparum* parasites (Fig.
296 6*A*). In stark contrast to this, however, the *P. berghei* promoter swap mutants responded to
297 drug treatment slightly earlier and disappeared from the circulation much more rapidly than
298 WT parasites (Fig. 6*B*). A similar phenotype was observed upon treatment of infected mice
299 with the artemisinin derivative artesunate, also previously been implicated in haem
300 sequestration, although this remains contentious (37-41) (Fig. 6*C*). Most surprisingly, we also
301 observed marked hypersensitivity of the *P. berghei* mutants towards atovaquone, a compound
302 that targets the parasite's mitochondrial electron transport chain (Fig. 6*D*), as well as a slight
303 but non-significant increase in sensitivity towards the antifolate sulfadoxin (Fig. 6*E*). The
304 relative survival levels of *pv5::5'ptex88* and *pv5::5'hsp101* on the fourth day of drug treatment
305 suggested the greatest degree of hypersensitivity towards chloroquine (2.1% and 1.4% of WT
306 survival, respectively), followed by atovaquone (3.5% and 8.6%) and artesunate (4.4% and
307 9.9%), and eventually sulfadoxin (20.5% and 27.8%). An unrelated slow-growing *P. berghei*
308 mutant deficient in the maintenance of the mitochondrial membrane potential displayed normal
309 sensitivity towards atovaquone using the same internally controlled assay (42), indicating that
310 reduced parasite multiplication is unlikely to cause drug hypersensitivity. Collectively, these
311 results suggest that interference with *PV5* expression critically enhances vulnerability of the
312 parasite towards drug-mediated insult during *in vivo* blood infection.

313 **DISCUSSION**

314 In this work, we have demonstrated that Hz formation in malaria parasites involves a secreted
315 calycin family member called PV5. While transcriptional deregulation of *PV5* in *P. berghei*
316 resulted in protracted Hz elongation along a pre-existing crystal plane, multidirectional
317 branching was observed in the complete absence of PV5 in *P. falciparum*. Species differences
318 aside, the disparity between those two phenotypes can be explained by the unique
319 transcriptional dynamics observed in the *P. berghei* mutants. Here, the hyperactive crystal
320 elongation, that follows an initial phase of normal Hz growth, coincides with a substantial
321 increase in Pb*PV5* transcript abundance during late parasite development. In their
322 physiological context, PTEX88 and HSP101 are co-expressed as members of the same
323 protein complex with HSP101 being more abundant than PTEX88 (34, 43), as supported by
324 our qPCR analysis. Thus, the increased phenotypic severity in the *pv5::5'hsp101* mutant over
325 the *pv5::5'ptex88* mutant indicates that the deficiencies in Hz formation can be attributed to
326 late overexpression of PV5. Together with the chaotic Hz crystal branching observed in PV5-
327 deficient *P. falciparum* parasites, this leads us to propose that PV5 acts as a facilitator of
328 unidirectional Hz extension.

329 It is interesting to speculate on the mechanisms by which PV5 may partake in haem
330 biomineralization. In laboratory crystallization experiments, the extent of crystallographic
331 mismatch branching is highly dependent on the degree of solute supersaturation, with high
332 levels favouring the generation of novel crystal nuclei on the surface of the parent crystal (44).
333 By contrast, lower degrees of supersaturation usually promote the expansion of pre-existing
334 crystals (44). It is conceivable that PV5 might reduce the extent of haem supersaturation by
335 binding haem or haematin dimers, thereby moderating *de novo* Hz nucleation and promoting
336 unidirectional crystal elongation. This could explain the Hz branching upon loss of PV5 in *P.*
337 *falciparum* as well as the prolonged crystal elongation and reduced Hz production upon late
338 upregulation of *PV5* in the *P. berghei* mutants. In support of this model, some lipocalin family
339 members are known to specifically bind the haem degradation product biliverdin (45-47). Such
340 interactions are unlikely to occur within the predicted PV5 β-barrel due to spatial constraints.
341 However, although experimental validation for this is currently lacking, potential ligand binding
342 sites might be located at the predicted prominently exposed loop between the barrel's β-
343 strands 5 and 6 (Fig. 1*B*) or at the extended amino-terminus.

344 The crystal branching characterising PV5-deficient *P. falciparum* parasites could also
345 be elicited by non-haem impurities adsorbing onto the crystal surface where they would
346 generate novel nucleation sites (44). In this alternative functional model, PV5 could act to bind

347 these impurities to create a vacuolar environment permissive for proper biomineralization.
348 *Pf*PV5-deficient parasites maintain an intact FV with a trans-vacuolar proton gradient as
349 indicated by staining with Lysosensor Blue DND-167 (Fig. S5*A*). In the absence of indications
350 for FV membrane damage, differences in leakage of impurities from the parasite cytoplasm
351 can be dismissed. However, we cannot rule out the possibility that specific ions or organic
352 compounds are more abundant in the vacuolar matrix of PV5-deficient parasites.

353 While the exact biophysical mechanisms that govern PV5-mediated Hz
354 morphogenesis remain to be delineated, our results support a model of conventional
355 crystallization within the aqueous milieu of the parasite's digestive compartments. The distinct
356 changes in crystal morphology and branching behaviour in the *PV5* mutants concur with
357 established mineralogical phenomena and are difficult to reconcile with a lipid or protein-
358 mediated polymerization scenario.

359 The striking dual localization pattern of PV5 is suggestive of initial secretion into the
360 PV followed by endocytic uptake. Since we ruled out an involvement of PV5 in haemoglobin
361 ingestion and catabolism, the transient vacuolar swelling in the *P. berghei* mutants likely
362 reflects a secondary effect mediated by the grave deficiencies in haem sequestration.

363 Our previous experiments had indicated that Pb*PV5* is essential for the asexual blood
364 stage development of *P. berghei* (27), and the deregulation of Pb*PV5* transcription in the
365 mutants described here indeed led to a striking fitness cost during *in vivo* infection. By contrast,
366 complete ablation of Pf*PV5* in *P. falciparum* only resulted in a moderate fitness loss *in vitro*.
367 The apparent dispensability of Pf*PV5* is therefore puzzling, but can be resolved by the notion
368 that *in vitro* culture does not necessarily reflect all adversities encountered during host
369 infection. For instance, Hz-mediated stiffening of the residual body in the absence of PV5
370 might hinder the passage of infected cells through capillaries or through the inter-endothelial
371 slits of the spleen, a scenario that would result in parasite elimination only during *in vivo*
372 infection. Similarly, we observed enhanced drug susceptibility only in the *P. berghei* mutants.
373 Thus, it appears plausible, that any imbalance in haem biomineralization in the absence of
374 PV5 is compensated for under optimal culture conditions and unfolds its adverse effects only
375 during *in vivo* infection. We thus propose that the molecular mechanism by which PV5
376 regulates Hz formation might involve host factors that are not encountered in a cell culture
377 setting.

378 The observation of enhanced drug susceptibility in the Pb*PV5* mutants is in agreement
379 with the notion that aberrant haem biomineralization chemo-sensitizes parasites to partner
380 drugs. Although oxidative stress and lipid peroxidation remained unchanged upon deletion of

381 Pf*PV5* (Fig. S5*B*), the reduced Hz formation efficiency in the *PV5* mutants suggests elevated
382 haem concentrations within the parasite mediating the fitness loss and drug hypersensitivity.

383 Together, we provide the first conclusive evidence for a parasite factor mediating Hz
384 formation *in vivo*, called PV5. Since this *Plasmodium*-encoded member of the calycin
385 superfamily also governs the parasites' vitality and susceptibility towards drug-mediated insult
386 during blood infection, our observations reinforce Hz formation as an excellent pathway for
387 therapeutic intervention. The investigation of the malaria parasite's haem detoxification
388 machinery *in vivo*, as exemplified herein for PV5, will significantly improve our understanding
389 of this unique haem biomineralization process and holds great promise for the development
390 of novel malaria intervention strategies.

391 **MATERIALS & METHODS**

392 **Structure homology modelling.** Structure homology modelling was performed using the
393 SWISS-MODEL server (48). *Pf*PV5 (residues 35-214) was aligned to the experimentally
394 validated structure of *Ec*Blc (residues 27-175, PDB ID: 3MBT) (49), resulting in a GMQE value
395 of 0.39 and a QMEAN value of -5.48. Modelling was confirmed with I-TASSER (50), which
396 also identified *Ec*Blc (PDB ID: 2ACO) (51) as the most closely related structural analogue of
397 *Pf*PV5 with a TM score of 0.75. Due to a lack of sequence similarity, the structure of the
398 extended *Pf*PV5 amino-terminus was not modelled.

399 ***P. berghei* cultivation**. *P. berghei* parasites were propagated in SWISS mice under constant
400 drug pressure with pyrimethamine (70 mg/l in drinking water, ingested *ad libitum*, MP
401 Biomedicals) to avoid homology-induced reversion of the promoter swap mutants to the
402 original WT genotype. This was routinely checked by diagnostic PCR of genomic DNA as
403 shown in Figures S2 *A* and *B*. Drug pressure was withdrawn 5 days prior to experimentation
404 to avoid secondary effects of pyrimethamine treatment. Pyrimethamine-resistant Berred WT
405 parasites (52) were treated accordingly. All infection experiments were carried out in strict
406 accordance with the German 'Tierschutzgesetz in der Fassung vom 22. Juli 2009' and the
407 Directive 2010/63/EU of the European Parliament and Council 'On the protection of animals
408 used for scientific purposes'. The protocol was approved by the ethics committee of the Berlin
409 state authority ('Landesamt fur Gesundheit und Soziales Berlin', permit number G0294/15).

410 *P. berghei* growth was determined with the previously described intravital competition
411 assay (52). In short, 500 mCherry-fluorescent Berred WT and 500 GFP-fluorescent mutant
412 blood stage parasites were co-injected intravenously and parasitaemia was analysed daily by
413 flow cytometry. For drug sensitivity assays, $5x10^6$ WT and $5x10^6$ mutant parasites were co-
414 injected intravenously. Drug treatment as well as daily flow cytometric parasite detection were
415 commenced three days later (43). Mice were treated with curative doses of chloroquine (288
416 mg/l in drinking water, ingested *ad libitum*, Sigma Aldrich), atovaquone (1.44 mg/kg body
417 weight per day injected intraperitoneally; GlaxoSmithKline), artesunate (50 mg/kg body weight
418 per day injected intraperitoneally; Sigma Aldrich) or sulfadoxin (1.4 g/l in drinking water,
419 ingested *ad libitum*; Sigma Aldrich). Mixed blood stages and schizonts were purified by
420 nycodenz gradient centrifugation (53).

421 ***P. falciparum* cultivation**. *P. falciparum* parasites were propagated in type AB+ human red
422 blood cells at 90% N_2, 5% CO_2 and 5% O_2 at 37°C in RPMI 1640 containing AlbuMAXII
423 (Thermo Fisher Scientific) supplemented with 2 mM L-glutamine. Parasites were routinely

424 synchronized using a combination of percoll gradient centrifugation and sorbitol lysis and were
425 treated with 100 nM rapamycin, various concentrations of E64 or equivalent volumes of
426 dimethyl sulfoxide (DMSO) from the early ring stage onward. Growth assays were performed
427 as described previously (54) and parasitaemia as well as DNA content were measured by flow
428 cytometry using the nuclear dye SYBR Green (1:10,000; Thermo Fisher Scientific). For
429 invasion assays, mature schizonts were incubated at 2% initial parasitaemia under static or
430 shaking (120 rpm) conditions, as confirmed by flow cytometry. Parasitaemia was measured
431 again 24 hours after inoculation and the fold-change was calculated. For drug- and inhibitor-
432 response analyses, *pv5-3xHA:loxP* ring stage cultures at 0.5 – 2% parasitaemia were treated
433 with varying concentrations of chloroquine or E64 in the presence of DMSO or rapamycin in
434 a 96 well format. Parasitaemia was determined three days later and the fold-change was
435 calculated. E64 was washed out after 36 hours to allow for reinvasion. In addition, nuclear
436 SYBR Green fluorescence was determined by flow cytometry following 44 hours of continuous
437 E64 treatment.

438 **Generation and validation of transgenic *Plasmodium* parasites**. To generate the Pb*PV5*
439 promoter swap mutants, the amino-terminal sequence of Pb*PV5* (PBANKA_0826700) was
440 PCR-amplified and cloned into the B3D+ vector using BamHI and SacII. The promoters of
441 Pb*PTEX88* (PBANKA_0941300) or Pb*HSP101* (PBANKA_0931200) were then amplified and
442 cloned in front of the start codon using BamHI (Figure S1*A*). Vectors were linearized with BstBI
443 and transfected into GFP-fluorescent *P. berghei* Bergreen WT parasites, using standard
444 protocols (53, 55, 56). Transgenic parasites were selected for with pyrimethamine and isolated
445 by limiting dilution cloning. Pb*PV5* transcript abundance in the WT and the promoter swap
446 mutants was measured by quantitative real-time PCR (qPCR) and normalized to *Pb*18S rRNA.

447 The conditional Pf*PV5* knockout line was generated using established Cas9-mediated
448 techniques. In short, *P. falciparum* 3D7 parasites constitutively expressing DiCre (B11 line)
449 were co-transfected with a pDC2 guide plasmid inducing Cas9-mediated double strand
450 cleavage of the Pf*PV5* locus (PF3D7_0925900), together with a linearized repair template (57-
451 59) (Figure S3*A*). The template was generated by gene synthesis and contained 5' and 3'
452 homology arms and a re-codonised 3xHA-tagged Pf*PV5* sequence. The endogenous intron
453 of Pf*PV5* was replaced with an artificial intron containing a *loxP* site (58). A second *loxP*
454 sequence was introduced behind the Pf*PV5* stop codon. For live imaging of *Pf*PV5, mCherry
455 was cloned into the conditional knockout vector in frame with the re-codonised Pf*PV5*
456 sequence using AatII. Transgenic parasites were selected for with WR99210 and cloned by
457 limiting dilution, making use of a previously developed plaque assay (60). Primers used for

458 molecular cloning, diagnostic PCR, and qPCR are indicated in Figures 4*A*, S1*A* and S3*A* as
459 well as in Table S2.

460 **Fluorescence microscopy.** The transgenic *P. berghei* parasite line *pv5-tag-GFP*^{PV} (27) was
461 imaged live using an AxioImager Z2 epifluorescence microscope equipped with an AxioCam
462 MR3 camera (Zeiss). For mechanical parasite expansion, 1-2 µl of infected blood were
463 incubated under a 22 x 40 mm coverslip for several minutes until erythrocyte lysis became
464 apparent. *P. falciparum* parasites were imaged on an Eclipse Ni light microscope (Nikon) fitted
465 with a C11440 digital camera (Hamamatsu). Immunofluorescence analysis was performed
466 with *P. falciparum pv5-3xHA:loxP* parasites that were fixed in 4% formaldehyde using rat anti-
467 HA (1:500; Sigma Aldrich) and rabbit anti-SERA5 (1:500) (54) primary antibodies in
468 combination with appropriate fluorophore-coupled secondary antibodies (1:1,000; Thermo
469 Fisher Scientific). Stainings with Lysosensor Blue DND-167 (Thermo Fisher Scientific),
470 BODIPY 581/591 C11 (Image-iT Lipid Peroxidation Kit, Thermo Fisher Scientific) and
471 CellROX Green (Thermo Fisher Scientific) were performed according to the manufacturer's
472 instructions.

473 **Scanning electron microscopy.** Hz was isolated from nycodenz (*P. berghei*) or percoll (*P.*
474 *falciparum*) gradient-purified infected red blood cells. Cells were lysed in water at room
475 temperature for 20 minutes, followed by a 10-minute centrifugation step at 17,000 x *g*. The
476 pellet was resuspended in 2% SDS in water and centrifuged as above. Three more washing
477 steps with 2% SDS were then followed by three washing steps with distilled water, before the
478 crystals were resuspended and transferred onto round glass cover slips (12 mm), where they
479 were dried. Cover slips were mounted on SEM specimen stubs, sputter-coated, and then
480 imaged on a LEO 1430 (Zeiss) or on a Quanta FEG 250 scanning electron microscope
481 (Thermo Fisher Scientific).

482 **Transmission electron microscopy.** Infected erythrocytes were initially fixed in 2.5%
483 glutaraldehyde, embedded in beads of 2% agarose, fixed and contrasted with 1% osmium
484 tetroxide, and further contrasted *en bloc* using 0.5% uranyl acetate. Following dehydration in
485 a graded series of ethanol and propylene oxide, beads were embedded in epoxy resin and
486 cured at 60°C for at least 24 hours. 60 nm sections were made with a Reichert Ultracut S
487 ultramicrotome (Leica) using a diamond knife. Sections were retrieved on copper hexagonal
488 mesh grids, and stained with 2% uranyl acetate and Reynold's lead citrate before imaging on
489 an EM 900 transmission electron microscope (Zeiss) equipped with a wide-angle slow-scan
490 2K CCD camera (Tröndle Restlichtverstärkersysteme).

491 **Electron diffraction.** Purified Hz was added to glow-discharged Lacey carbon films on 400
492 mesh copper grids which were then transferred to a Vitrobot Mark IV plunge freezer (Thermo
493 Fisher Scientific) with 100% humidity at 7°C. The grids were blotted for 3 seconds with blot
494 force 1 and plunge frozen in liquid ethane cooled by liquid nitrogen. Electron diffraction data
495 were collected on a Talos cryo-electron microscope (Thermo Fisher Scientific) operated at
496 200 keV equipped with a hybrid pixel Timepix detector (512 x 512 pixels, 55 x 55 µm pixel
497 size; Amsterdam Scientific Instruments). Still and rotation (70°) datasets were collected with
498 a beam size of 2 µm. The recording time varied between 15 and 100 seconds. To determine
499 the resolution, a powder pattern of an aluminum diffraction standard was recorded. Since the
500 Hz crystals had a strong tendency to stick together, we measured diffraction data of crystal
501 clusters. For each individual data set, we determined the location of the central electron beam
502 and shifted the patterns to make the beams coincide. Since crystal clustering prevented
503 indexing of the diffraction data, the radial median and maximum intensities were determined
504 as a function of resolution. Hereafter, the WT and *pv5::5'hsp101* datasets were averaged and
505 normalized to the local background median intensity at 0.18 $Å^{-1}$.

506 **Subcellular fractionation and immunoblotting.** *P. falciparum* parasites were released from
507 erythrocytes by treatment with 0.15% saponin in PBS. Murine erythrocytes infected with
508 the *pv5-tag-GFP*^{PV} or *exp2-mCherry P. berghei* lines (64) were purified on a nycodenz
509 gradient and lysed hypotonically for 1 hour on ice in 10 mM TRIS-HCl, pH 7.5. *P. berghei*
510 lysates were spun 50 minutes at 100,000 × *g*. Membrane pellets were resuspended in 0.1 M
511 Na_2CO_3 in PBS or in 1% Triton X-100 in PBS, respectively, and spun 50 minutes at
512 100,000 × *g*. Proteins were separated on SDS-polyacrylamide and transferred onto a
513 nitrocellulose membrane. Western blotting was performed using rat anti-mCherry (1:5,000;
514 ChromoTek), chicken anti-GFP (1:5,000; Abcam), rat anti-HA (1:1,000, Sigma Aldrich), rat
515 anti-*Pf*BiP (1:1,000) (62) and rabbit anti-human-haemoglobin-α primary antibodies (1:1,000,
516 Abcam) followed by chemiluminescence detection with horseradish peroxidase-coupled
517 secondary antibodies (1:10,000; Sigma Aldrich, or 1:5,000, Jackson ImmunoResearch).

518 **Quantitative haemozoin analysis.** Hz was visualized and quantified by microscopy of
519 methanol-fixed infected red blood cells. Hz from *P. berghei* was analysed by reflection contrast
520 polarized light microscopy using a Leica DMR widefield microscope equipped with a ProgRes
521 MF camera (Jenoptik) and the POL filter set 513813 (Leica). Hz from *P. falciparum* was
522 analysed by transmitted polarized light (488 nm) microscopy using an LSM 710 confocal
523 microscope (Zeiss) equipped with a crossed polarizer in the condenser. Cellular granularity
524 was approximated by quantification of side scattered light using an LSRFortessa flow
525 cytometer (BD Biosciences). Hz crystal dimensions were analysed using FIJI. Due to the

526 variation in the *P. berghei* mutant's crystal width, individual crystals were divided into nine
527 evenly spaced segments along the dominant axis. The width of each segment was determined
528 and the values were averaged. For the *pv5::5'hsp101* parent crystal and the crystal outgrowth,
529 transects were drawn through the central axis of either structure and their shared angle was
530 determined. Hz movement within the FV of *pv5-3xHA:loxP* parasites was imaged live 36 hours
531 following treatment with DMSO or rapamycin, respectively.

532 **REFERENCES**

533 1. A. G. Maier, K. Matuschewski, M. Zhang, M. Rug, *Plasmodium falciparum*. *Trends*
534 *Parasitol* **35**, 481-482 (2019).

535 2. P. A. Sigala, D. E. Goldberg, The peculiarities and paradoxes of *Plasmodium* heme
536 metabolism. *Annu Rev Microbiol* **68**, 259-278 (2014).

537 3. V. L. Lew, T. Tiffert, H. Ginsburg, Excess hemoglobin digestion and the osmotic
538 stability of *Plasmodium falciparum*-infected red blood cells. *Blood* **101**, 4189-4194
539 (2003).

540 4. D. E. Goldberg, A. F. Slater, A. Cerami, G. B. Henderson, Hemoglobin degradation in
541 the malaria parasite *Plasmodium falciparum*: an ordered process in a unique organelle.
542 *Proc Natl Acad Sci U S A* **87**, 2931-2935 (1990).

543 5. C. Slomianny, G. Prensier, P. Charet, [Comparative ultrastructural study of the process
544 of hemoglobin degradation by *P. berghei* (Vincke and Lips, 1948) as a function of the
545 state of maturity of the host cell]. *J Protozool* **32**, 1-5 (1985).

546 6. A. R. Dluzewski *et al.*, Formation of the food vacuole in *Plasmodium falciparum*: a
547 potential role for the 19 kDa fragment of merozoite surface protein 1 (MSP1(19)). *PLoS*
548 *One* **3**, e3085 (2008).

549 7. S. Kumar, U. Bandyopadhyay, Free heme toxicity and its detoxification systems in
550 human. *Toxicol Lett* **157**, 175-188 (2005).

551 8. S. Pagola, P. W. Stephens, D. S. Bohle, A. D. Kosar, S. K. Madsen, The structure of
552 malaria pigment beta-haematin. *Nature* **404**, 307-310 (2000).

553 9. A. F. Slater *et al.*, An iron-carboxylate bond links the heme units of malaria pigment.
554 *Proc Natl Acad Sci U S A* **88**, 325-329 (1991).

555 10. I. Weissbuch, L. Leiserowitz, Interplay between malaria, crystalline hemozoin
556 formation, and antimalarial drug action and design. *Chem Rev* **108**, 4899-4914 (2008).

557 11. M. Olivier, K. Van Den Ham, M. T. Shio, F. A. Kassa, S. Fougeray, Malarial pigment
558 hemozoin and the innate inflammatory response. *Front Immunol* **5**, 25 (2014).

559 12. T. J. Egan, W. W. Mavuso, K. K. Ncokazi, The mechanism of beta-hematin formation
560 in acetate solution. Parallels between hemozoin formation and biomineralization
561 processes. *Biochemistry* **40**, 204-213 (2001).

562 13. T. J. Egan, D. C. Ross, P. A. Adams, Quinoline anti-malarial drugs inhibit spontaneous
563 formation of beta-haematin (malaria pigment). *FEBS Lett* **352**, 54-57 (1994).

564 14. M. M. Chen, L. Shi, D. J. Sullivan, Jr., *Haemoproteus* and *Schistosoma* synthesize
565 heme polymers similar to *Plasmodium* hemozoin and beta-hematin. *Mol Biochem*
566 *Parasitol* **113**, 1-8 (2001).

567 15. A. Dorn, R. Stoffel, H. Matile, A. Bubendorf, R. G. Ridley, Malarial haemozoin/beta-
568 haematin supports haem polymerization in the absence of protein. *Nature* **374**, 269-
569 271 (1995).

570 16. D. Jani *et al.*, HDP – a novel heme detoxification protein from the malaria parasite.
571 *PLoS Pathog* **4**, e1000053 (2008).

572 17. D. J. Sullivan, Jr., I. Y. Gluzman, D. E. Goldberg, *Plasmodium* hemozoin formation
573 mediated by histidine-rich proteins. *Science* **271**, 219-222 (1996).

574 18. A. F. Slater, A. Cerami, Inhibition by chloroquine of a novel haem polymerase enzyme
575 activity in malaria trophozoites. *Nature* **355**, 167-169 (1992).

576 19. A. N. Hoang, R. D. Sandlin, A. Omar, T. J. Egan, D. W. Wright, The neutral lipid
577 composition present in the digestive vacuole of *Plasmodium falciparum* concentrates
578 heme and mediates beta-hematin formation with an unusually low activation energy.
579 *Biochemistry* **49**, 10107-10116 (2010).

580 20. M. A. Ambele, T. J. Egan, Neutral lipids associated with haemozoin mediate efficient
581 and rapid beta-haematin formation at physiological pH, temperature and ionic
582 composition. *Malar J* **11**, 337 (2012).

583 21. J. M. Pisciotta *et al.*, The role of neutral lipid nanospheres in *Plasmodium falciparum*
584 haem crystallization. *Biochem J* **402**, 197-204 (2007).

585 22. D. J. Sullivan, Jr., I. Y. Gluzman, D. G. Russell, D. E. Goldberg, On the molecular
586 mechanism of chloroquine's antimalarial action. *Proc Natl Acad Sci U S A* **93**, 11865-
587 11870 (1996).

588 23. K. N. Olafson, T. Q. Nguyen, J. D. Rimer, P. G. Vekilov, Antimalarials inhibit hematin
589 crystallization by unique drug-surface site interactions. *Proc Natl Acad Sci U S A* **114**,
590 7531-7536 (2017).

591 24. T. Herraiz, H. Guillen, D. Gonzalez-Pena, V. J. Aran, Antimalarial quinoline drugs
592 inhibit beta-hematin and increase free hemin catalyzing peroxidative reactions and
593 inhibition of cysteine proteases. *Sci Rep* **9**, 15398 (2019).

594 25. S. N. Cohen, K. O. Phifer, K. L. Yielding, Complex formation between chloroquine and
595 ferrihaemic acid *in vitro*, and its effect on the antimalarial action of chloroquine. *Nature*
596 **202**, 805-806 (1964).

597 26. U. D'Alessandro, H. Buttiens, History and importance of antimalarial drug resistance.
598 *Trop Med Int Health* **6**, 845-848 (2001).

599 27. J. M. Matz, K. Matuschewski, An *in silico* down-scaling approach uncovers novel
600 constituents of the *Plasmodium*-containing vacuole. *Sci Rep* **8**, 14055 (2018).

601 28. D. R. Flower, The lipocalin protein family: structure and function. *Biochem J* **318 (Pt**
602 **1)**, 1-14 (1996).

603 29. D. R. Flower, A. C. North, C. E. Sansom, The lipocalin protein family: structural and
604 sequence overview. *Biochim Biophys Acta* **1482**, 9-24 (2000).

605 30. H. E. Bullen *et al.*, Biosynthesis, localization, and macromolecular arrangement of the
606 *Plasmodium falciparum* translocon of exported proteins (PTEX). *J Biol Chem* **287**,
607 7871-7884 (2012).

608 31. M. Morita *et al.*, PV1, a novel *Plasmodium falciparum* merozoite dense granule protein,
609 interacts with exported protein in infected erythrocytes. *Sci Rep* **8**, 3696 (2018).

610 32. H. Iriko *et al.*, *Plasmodium falciparum* exported protein 1 is localized to dense granules
611 in merozoites. *Parasitol Int* **67**, 637-639 (2018).

612 33. M. Lamarque *et al.*, Food vacuole proteome of the malarial parasite *Plasmodium*
613 *falciparum*. *Proteomics Clin Appl* **2**, 1361-1374 (2008).

614 34. T. D. Otto *et al.*, A comprehensive evaluation of rodent malaria parasite genomes and
615 gene expression. *BMC Biol* **12**, 86 (2014).

616 35. J. M. Matz *et al.*, *In vivo* function of PTEX88 in malaria parasite sequestration and
617 virulence. *Eukaryot Cell* **14**, 528-534 (2015).

618 36. M. Zhang *et al.*, Uncovering the essential genes of the human malaria parasite
619 *Plasmodium falciparum* by saturation mutagenesis. *Science* **360** (2018).

620 37. Y. L. Hong, Y. Z. Yang, S. R. Meshnick, The interaction of artemisinin with malarial
621 hemozoin. *Mol Biochem Parasitol* **63**, 121-128 (1994).

622 38. R. K. Haynes *et al.*, Artemisinin antimalarials do not inhibit hemozoin formation.
623 *Antimicrob Agents Chemother* **47**, 1175 (2003).

624 39. W. Asawamahasakda, I. Ittarat, C. C. Chang, P. McElroy, S. R. Meshnick, Effects of
625 antimalarials and protease inhibitors on plasmodial hemozoin production. *Mol*
626 *Biochem Parasitol* **67**, 183-191 (1994).

627 40. A. V. Pandey, B. L. Tekwani, R. L. Singh, V. S. Chauhan, Artemisinin, an endoperoxide
628 antimalarial, disrupts the hemoglobin catabolism and heme detoxification systems in
629 malarial parasite. *J Biol Chem* **274**, 19383-19388 (1999).

630 41. N. Basilico, E. Pagani, D. Monti, P. Olliaro, D. Taramelli, A microtitre-based method
631 for measuring the haem polymerization inhibitory activity (HPIA) of antimalarial drugs.
632 *J Antimicrob Chemother* **42**, 55-60 (1998).

633 42. T. F. de Koning-Ward *et al.*, A newly discovered protein export machine in malaria
634 parasites. *Nature* **459**, 945-949 (2009).

635 43. J. M. Matz, C. Goosmann, K. Matuschewski, T. W. A. Kooij, An unusual prohibitin
636 regulates malaria parasite mitochondrial membrane potential. *Cell Rep* **23**, 756-767
637 (2018).

638 44. X. Y. Liu, "Heterogeneous nucleation and crystal network formation" in Crystal growth
639 of technologically important electronic materials, K. Byrappa, T. Ohachi, H. Klapper,
640 R. Fornari, Eds. (Allied Publishers PVT. Limited, New Delhi, 2003), pp. 118-135.

641 45. R. Huber *et al.*, Molecular structure of the bilin binding protein (BBP) from *Pieris*
642 *brassicae* after refinement at 2.0 Å resolution. *J Mol Biol* **198**, 499-513 (1987).

643 46. R. Huber *et al.*, Crystallization, crystal structure analysis and preliminary molecular
644 model of the bilin binding protein from the insect *Pieris brassicae*. *J Mol Biol* **195**, 423-
645 434 (1987).

646 47. H. M. Holden, W. R. Rypniewski, J. H. Law, I. Rayment, The molecular structure of
647 insecticyanin from the tobacco hornworm *Manduca sexta* L. at 2.6 Å resolution. *EMBO*
648 *J* **6**, 1565-1570 (1987).

649 48. A. Waterhouse *et al.*, SWISS-MODEL: homology modelling of protein structures and
650 complexes. *Nucleic Acids Res* **46**, W296-W303 (2018).

651 49. A. Schiefner, L. Chatwell, D. A. Breustedt, A. Skerra, Structural and biochemical
652 analyses reveal a monomeric state of the bacterial lipocalin Blc. *Acta Crystallogr D Biol*
653 *Crystallogr* **66**, 1308-1315 (2010).

654 50. J. Yang, Y. Zhang, Protein structure and function prediction using I-TASSER. *Curr*
655 *Protoc Bioinformatics* **52**, 5 8 1-5 8 15 (2015).

656 51. V. Campanacci, R. E. Bishop, S. Blangy, M. Tegoni, C. Cambillau, The membrane
657 bound bacterial lipocalin Blc is a functional dimer with binding preference for
658 lysophospholipids. *FEBS Lett* **580**, 4877-4883 (2006).

659 52. J. M. Matz, K. Matuschewski, T. W. Kooij, Two putative protein export regulators
660 promote *Plasmodium* blood stage development *in vivo*. *Mol Biochem Parasitol* **191**,
661 44-52 (2013).

662 53. C. J. Janse *et al.*, High efficiency transfection of *Plasmodium berghei* facilitates novel
663 selection procedures. *Mol Biochem Parasitol* **145**, 60-70 (2006).

664 54. R. Stallmach *et al.*, *Plasmodium falciparum* SERA5 plays a non-enzymatic role in the
665 malarial asexual blood-stage lifecycle. *Mol Microbiol* **96**, 368-387 (2015).

666 55. J. M. Matz, T. W. Kooij, Towards genome-wide experimental genetics in the *in vivo*
667 malaria model parasite *Plasmodium berghei*. *Pathog Glob Health* **109**, 46-60 (2015).

668 56. T. W. Kooij, M. M. Rauch, K. Matuschewski, Expansion of experimental genetics
669 approaches for *Plasmodium berghei* with versatile transfection vectors. *Mol Biochem*
670 *Parasitol* **185**, 19-26 (2012).

671 57. C. R. Collins *et al.*, Robust inducible Cre recombinase activity in the human malaria
672 parasite *Plasmodium falciparum* enables efficient gene deletion within a single asexual
673 erythrocytic growth cycle. *Mol Microbiol* **88**, 687-701 (2013).

674 58. M. L. Jones *et al.*, A versatile strategy for rapid conditional genome engineering using
675 *loxP* sites in a small synthetic intron in *Plasmodium falciparum*. *Sci Rep* **6**, 21800
676 (2016).

677 59. E. Knuepfer, M. Napiorkowska, C. van Ooij, A. A. Holder, Generating conditional gene
678 knockouts in *Plasmodium* – a toolkit to produce stable DiCre recombinase-expressing
679 parasite lines using CRISPR/Cas9. *Sci Rep* **7**, 3881 (2017).

680 60. J. A. Thomas *et al.*, Development and application of a simple plaque assay for the
681 human malaria parasite *Plasmodium falciparum*. *PLoS One* **11**, e0157873 (2016).

682 61. J. M. Matz *et al.*, The *Plasmodium berghei* translocon of exported proteins reveals
683 spatiotemporal dynamics of tubular extensions. *Sci Rep* **5**, 12532 (2015).

684 62. E. Knuepfer *et al.*, RON12, a novel *Plasmodium*-specific rhoptry neck protein important
685 for parasite proliferation. *Cell Microbiol* **16**, 657-672 (2014).

686 63. R. Buller, M. L. Peterson, Ö. Almarsson, L. Leiserowitz, Quinoline binding site on
687 malaria pigment crystal: a rational pathway for antimalaria drug design. *Cryst Growth*
688 *Des* **2**, 553-562 (2002).

689 64. J. Friesen *et al.*, Natural immunization against malaria: causal prophylaxis with
690 antibiotics. *Sci Transl Med* **2**, 40ra49 (2010).

691 **AUTHOR CONTRIBUTIONS**

692 JMM conceived the study and performed all experiments requiring genetic manipulation and
693 cultivation of *P. berghei* and *P. falciparum* parasites. JMM, BD, AB, PM, TS and LC contributed
694 to Hz analysis by SEM and TEM. TBB, EvG and JPA performed and analysed electron
695 diffraction experiments. KM and MJB contributed to data interpretation. The manuscript was
696 written by JMM with input from TBB, EvG, JPA, KM and MJB.

697 **ACKNOWLEDGEMENTS**

698 We thank Volker Brinkmann and Christian Goosmann (Max Planck Institute for Infection
699 Biology, Berlin) as well as Kurt Anderson (The Francis Crick Institute, London) for assistance
700 with polarization microscopy. We also thank Darren Flower (Aston University, Birmingham)
701 and Leslie Leiserowitz (Weizmann Institute of Science, Rehovot) for fruitful discussion. This
702 work was supported by a stipend from the Deutsche Forschungsgemeinschaft (DFG, project
703 number 419345764 to JMM) and in part by funding to JMM, LC, AB and MJB from the Francis
704 Crick Institute, which receives its core funding from Cancer Research UK (FC001043), the UK
705 Medical Research Council (FC001043), and the Wellcome Trust (FC001043). JMM, BD, PM,
706 TS and KM were also supported by the Humboldt University and by the Alliance Berlin
707 Canberra ‘‘Crossing Boundaries: Molecular Interactions in Malaria’’, which is co-funded by a
708 grant from the DFG for the International Research Training Group (IRTG) 2290 and the
709 Australian National University. We further acknowledge funding from the Swiss National
710 Science Foundation (project 31003A_17002 to TBB and project 200021_165669 to TBB and
711 JPA). We thank the Center for Cellular Imaging and NanoAnalytics for support and use of the
712 cryo-electron microscope.

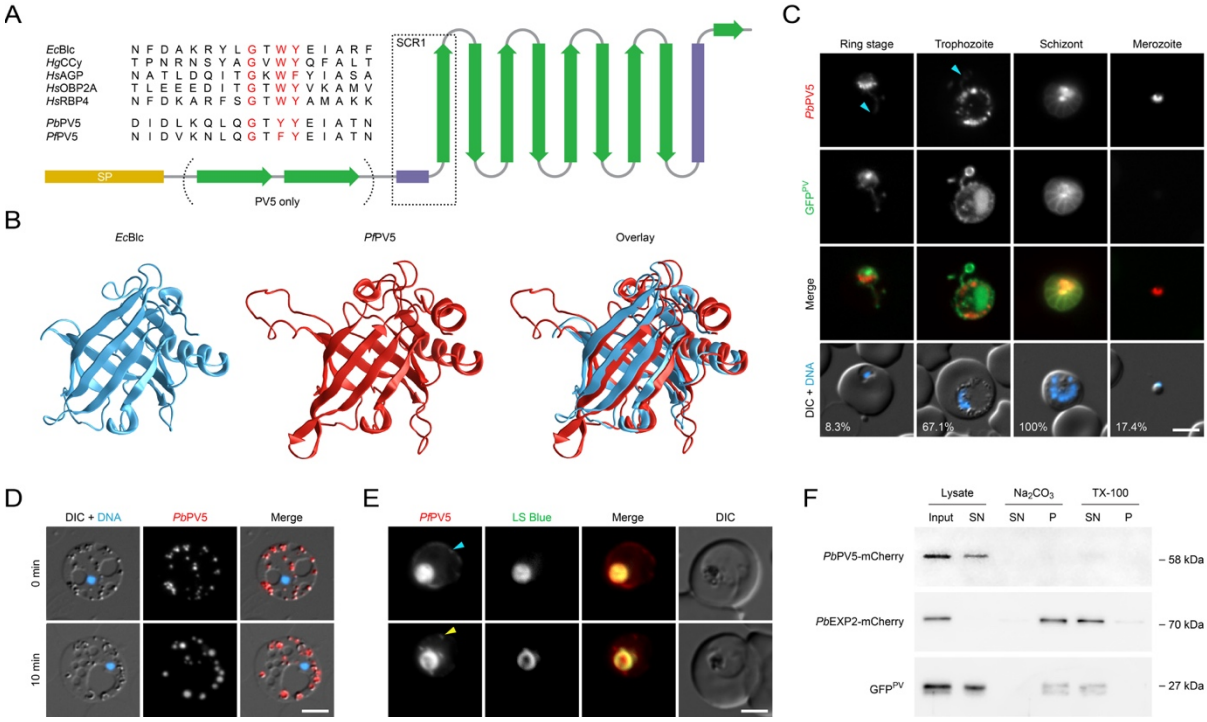

Fig. 1. The *Plasmodium* lipocalin PV5 is trafficked to the parasite's digestive compartments.

(*A*) PV5 is a lipocalin family member. Secondary structure of *Plasmodium* PV5. Yellow, signal peptide (SP); green, ß-strands; purple, α-helices. Note the two amino-terminal ß-strands specific to PV5. Alignments of the structurally conserved region 1 (SCR1) from different lipocalin family members and PV5 are shown in the upper left corner. Signature residues are highlighted in red. *Ec*Blc, *Escherichia coli* bacterial lipocalin; *Hg*CCy; *Homarus gammarus* (European lobster) crustacyanin; *Hs*AGP, *Homo sapiens* α_1-acid glycoprotein; *Hs*OBP2A, *H. sapiens* odorant-binding protein 2A; *Hs*RBP4, *H. sapiens* retinol-binding protein 4; *Pb*/*Pf*PV5, PV5 from *P. berghei* and *P. falciparum*.

(*B*) Structure homology modelling predicts a lipocalin fold for *Pf*PV5. Shown are the experimentally validated structure of *Ec*Blc (blue, left, residues 27-175, PDB ID: 3MBT), the derived model of *Pf*PV5 (red, centre, residues 35-214) using *Ec*Blc as a homology template, and an overlay (right). Modelling was performed with SWISS-MODEL and supported by I-TASSER. Amino acid sequence identity is 20%, similarity calculated from BLOSUM62 substitution matrix is 0.3.

(*C*) Dual protein localization of PV5 to extensions of the PV and to intraparasitic structures in *P. berghei*. Transgenic parasites expressing the PV marker GFP^{PV} and the endogenous Pb*PV5* gene fused to mCherry-3xMyc were imaged live (27). Shown are the mCherry (red, first row) and GFP channels (green, second row), a merge of both signals (third row) and a merge of differential interference contrast images (DIC) and Hoechst 33342 nuclear stain (blue, fourth row). Cyan arrowheads, *Pb*PV5 in PV tubules. Numbers represent normalized

735 mCherry intensity values obtained by quantitative live fluorescence microscopy. N=44
736 parasites.

737 (*D*) Intraparasitic PV5 localizes to Hz-containing DVs in *P. berghei*. Parasites were
738 incubated in 1-2 µl under a large coverslip (22 x 40 mm) for several minutes, leading to lysis
739 of the host erythrocyte and the PV, and to mechanical expansion of the parasite (top). Shown
740 are a merge of DIC and Hoechst 33342 nuclear stain (blue, first row), the signal of tagged
741 *Pb*PV5 (red, second row), as well as a merge of all three channels (third row). Swelling of
742 *Pb*PV5-containing DVs was observed ten minutes later (bottom). Note the even distribution of
743 *Pb*PV5 throughout the swollen DVs.

744 (*E*) PV5 localizes to the central FV, intraparasitic vesicles and to the PV in *P. falciparum*.
745 Transgenic parasites expressing the endogenous Pf*PV5* gene fused to mCherry were imaged
746 live in the presence of Lysosensor Blue DND-167 (LS Blue). Shown are the signals of mCherry
747 (red, first row), LS Blue (green, second row), a merge of both signals (third row), and DIC
748 images (fourth row). Cyan arrowhead, *Pf*PV5 in PV (top). Yellow arrowhead, *Pf*PV5 in small
749 intraparasitic vesicles (bottom). Bars, 5 µm.

750 (*F*) PV5 is a soluble protein. Subcellular fractionation was performed using the *Pb*PV5-
751 tagged *P. berghei* line, which also expresses the soluble marker GFP^{PV}, and a *P. berghei* line
752 expressing the transmembrane protein *Pb*EXP2 fused to mCherry-3xMyc (64). Cell lysates
753 were centrifuged and resultant membrane pellets were subjected to solubilization with Na_2CO_3
754 and Triton X-100 (TX-100). Input, supernatant (SN) and pellet fractions (P) were analysed by
755 Western blot using anti-mCherry and anti-GFP primary antibodies.

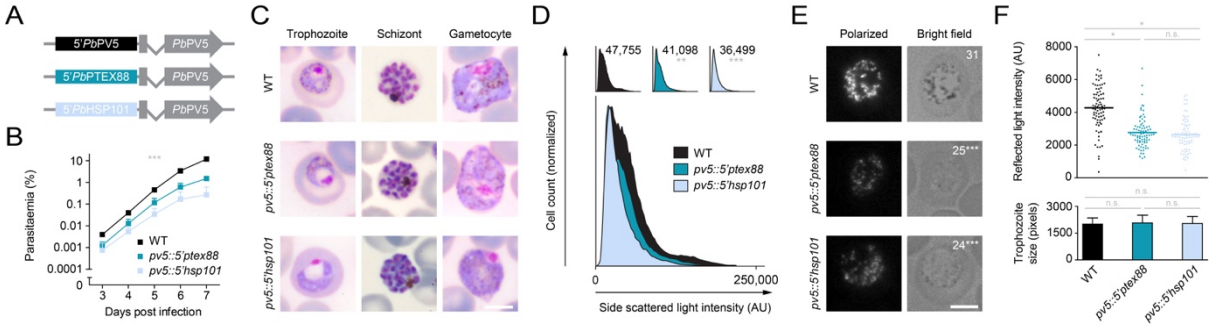

Fig. 2. Deregulated expression of *PV5* impacts haemozoin formation in *Plasmodium berghei.*

(*A*) Schematic representation of the genotypes of WT (top) and transgenic *pv5::5'ptex88* (middle) and *pv5::5'hsp101* parasites (bottom). In the mutants, the endogenous Pb*PV5* promoter (black) was exchanged for the promoter of Pb*PTEX88* (dark blue) or Pb*HSP101* (light blue), respectively.

(*B*) Reduced parasite proliferation upon *Pb*PV5 promoter swapping. Asexual blood stage development was analysed using the intravital competition assay (55). Average parasite multiplication rates were 11.4 (WT), 9.1 (*pv5::5'ptex88*) and 6.2 (*pv5::5'hsp101*). Shown are mean values +/- SD. ***, P<0.001; Two-way ANOVA. N=3 independent infections.

(*C*) Morphology of trophozoite, schizont and gametocyte stages in the WT, *pv5::5'ptex88* and *pv5::5'hsp101* lines as observed by Giemsa staining. Note the lack of prominent dark pigment granules in mutant trophozoites and gametocytes as well as the dilation of the FV in mutant trophozoites. Bar, 5 µm.

(*D*) Pb*PV5* promoter swap mutants are less granular. Infected blood was subjected to flow cytometry and the intensity of the side scattered light was determined. Shown are individual histograms including the mean side scatter intensity values (top) as well as a merge of WT, *pv5::5'ptex88* and *pv5::5'hsp101* histograms (bottom). Significances are shown for the comparison of the mutants with WT. n.s., non-significant; **, P<0.01; ***, P<0.001; One-way ANOVA and Tukey's multiple comparison test. N=6 independent infections.

(*E, F*) Pb*PV5* is required for efficient Hz formation. (*E*) Trophozoites were visualized by polarization microscopy (left) and bright field imaging (right). Numbers indicate the mean quantity of bright puncta in polarization images. Significances are shown for the comparison of the mutants with WT. Bar, 5 µm. (*F*) Quantitative polarization microscopy. Depicted are individual and mean intensity values of reflected polarized light in methanol-fixed WT, *pv5::5'ptex88* and *pv5::5'hsp101* trophozoites (bars, upper graph). Only trophozoites of similar size were analysed (lower graph). Depicted are mean values +/- SD. n.s., non-significant; *, P<0.05; ***, P<0.001; One-way ANOVA and Tukey's multiple comparison test. N=80 trophozoites from 4 independent infections.

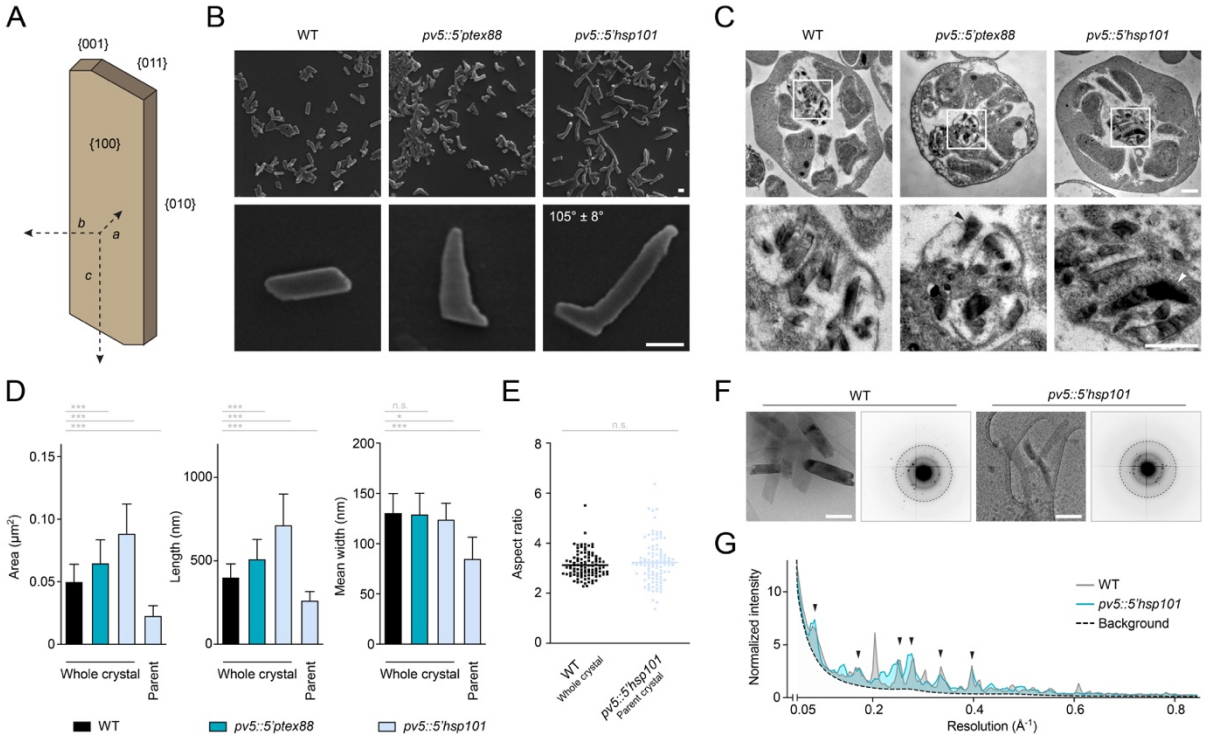

Fig. 3. PV5 determines haemozoin morphology in *Plasmodium berghei.*

(A) Hz crystal architecture. In *Plasmodium* WT parasites, Hz assembles as triclinic high aspect ratio parallelograms (63). Characteristic crystal axes and faces are indicated.

(*B*) Scanning electron micrographs of Hz purified from WT, *pv5::5'ptex88* and *pv5::5'hsp101* mixed blood stage parasites. The angle between the regularly shaped *pv5::5'hsp101* parent crystal and the outgrowth is indicated. N=130 crystals. Bars, 100 nm.

(*C*) Crystal morphology *in situ*. Shown are TEM images of WT, *pv5::5'ptex88* and *pv5::5'hsp101* schizonts (top) as well as their residual body at higher magnification (bottom). Abnormal crystal shapes in the mutants are indicated by arrowheads. Bars, 500 nm.

(*D*) Hyperactive Hz growth is unidirectional. Shown are the dimensions of whole individual Hz crystals extracted from WT, *pv5::5'ptex88* and *pv5::5'hsp101* parasites including the area exposed to the electron beam (left) as well as the length (centre) and mean width of the crystals (right). The theoretical dimensions of the *pv5::5'hsp101* parent crystal were interpolated and are depicted as well. Shown are mean values +/- SD. n.s., non-significant; *, P<0.05; ***, P<0.001; One-way ANOVA and Tukey's multiple comparison test. N=100 crystals.

(*E*) Normal aspect ratio of *pv5::5'hsp101* parent crystals. Shown are the aspect ratios of whole Hz crystals from WT parasites and of the parent crystal from *pv5::5'hsp101*-generated

804 Hz. Depicted are individual and mean values (bars). n.s., non-significant; Student's *t*-test.
805 N=100 crystals.

806 (*F, G*) Unaltered crystalline order in Hz of *pv5::5'hsp101* parasites. (*F*) Depicted are TEM
807 images (left) of Hz purified from WT and *pv5::5'hsp101* parasites as well as their
808 corresponding electron diffraction patterns (right) showing comparable resolution of the Bragg
809 peaks. Dashed circles demark a resolution of 0.5 $Å^{-1}$. Bars, 200 nm. (*G*) Plot of the radial
810 maximum diffracted intensity as a function of resolution. Data were normalized to the average
811 median intensity at 0.18 $Å^{-1}$, in order to correct for differences in diffracted volume. Arrowheads
812 denote overlapping peaks. N=10 (WT) and 18 (*pv5::5'hsp101*) diffraction data sets.

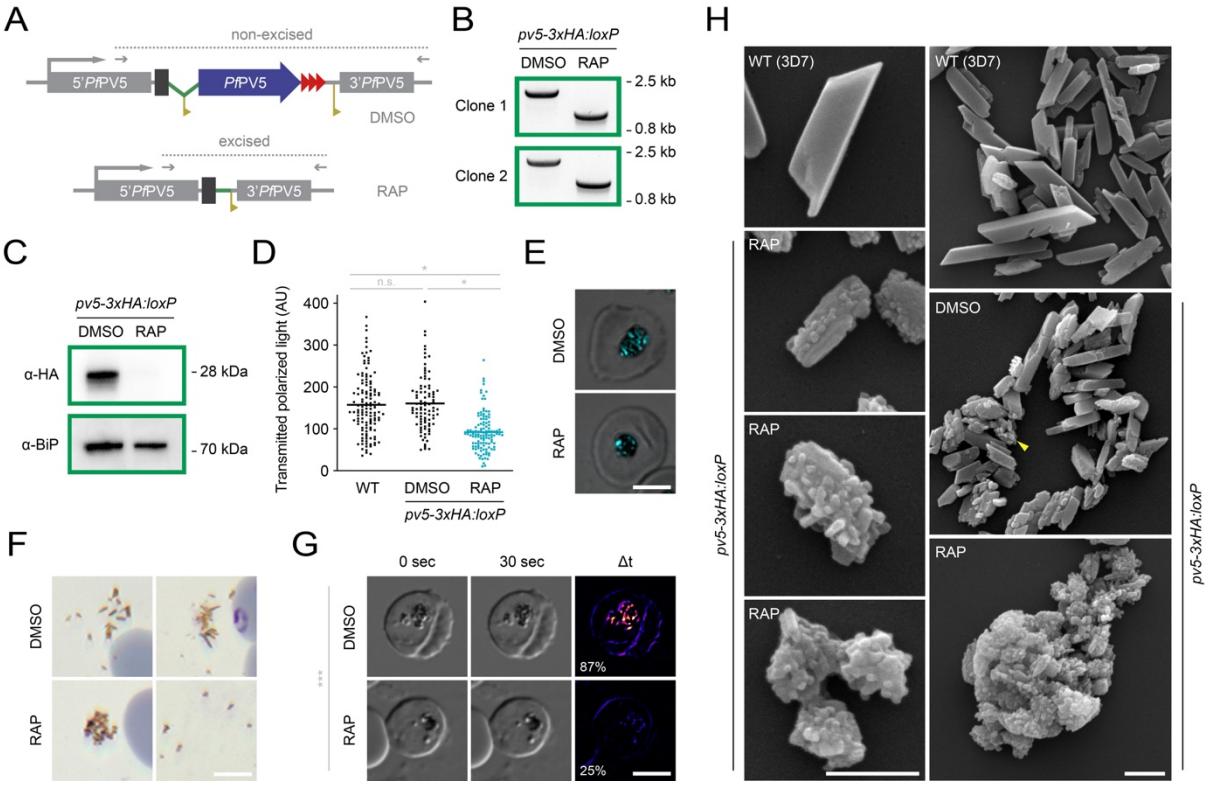

Fig. 4. Absence of PV5 causes haemozoin branching in *Plasmodium falciparum*.

(*A*) Schematic representation of DiCre-mediated Pf*PV5* excision. The endogenous locus was modified to introduce *loxP* sites (yellow) flanking the majority of the coding sequence of the 3xHA (red)-tagged *Pf*PV5 (blue). The artificial intron is indicated in green. See also Fig. S3*A*. Treatment with rapamycin (RAP) induces Cre recombinase-mediated excision of the *loxP*-flanked sequence which results in truncation of Pf*PV5* leaving behind only the sequence encoding the protein's signal peptide. Excision-sensitive primer combinations are indicated by arrows and expected diagnostic PCR fragments by dotted lines.

(*B*) Diagnostic PCR of the modified Pf*PV5* locus following treatment with dimethyl sulfoxide (DMSO) or RAP, respectively, using the primer combinations depicted in *A*. Results are shown from two independent *pv5-3xHA:loxP* clones.

(*C*) Loss of *Pf*PV5 protein. Western blot analysis of parasite extracts following treatment with DMSO or RAP, respectively, using anti-HA and anti-*Pf*BiP primary antibodies.

(*D*, *E*) *Pf*PV5 is required for efficient Hz formation. WT and *pv5-3xHA:loxP* parasites were treated with DMSO or RAP, respectively, and visualized by polarization microscopy 36 hours after invasion. (*D*) Quantification of the polarized light intensity. Depicted are values from individual parasites as well as the mean intensity values (bars). n.s., non-significant; *, P<0.05; One-way ANOVA and Tukey's multiple comparison test. N≥93 parasites from 3 independent experiments. (*E*) Exemplary images of DMSO- and RAP-treated *pv5-3xHA:loxP* parasites.

833 Shown is a merge of polarized light (cyan) and DIC. Bar, 5 µm.

834 (*F*) Abnormal Hz morphology in the absence of *Pf*PV5. Hz released from residual bodies
835 during parasite egress was imaged in Giemsa-stained thin culture smears of DMSO and RAP-
836 treated *pv5-3xHA:loxP* parasites. Note the spreading of elongated Hz crystals in DMSO-
837 treated cultures and the clumping of granular Hz upon RAP treatment (left). Only in very few
838 instances did the crystals detach from one another in RAP-treated cultures (right). Bar, 5 µm.

839 (*G*) Reduced Hz movement in the FV upon loss of *Pf*PV5. Shown are DIC images of live
840 DMSO and RAP-treated *pv5-3xHA:loxP* parasites 36 hours after invasion. Parasites were
841 imaged twice at an interval of 30 seconds (left and centre) and the difference of both images
842 was visualized with pixel-by-pixel intensity subtraction (right). Note the absence of Hz
843 movement in the RAP-treated parasite (see also Movie S1). The percentage of parasites with
844 moving Hz is indicated. ***, P<0.001; Student's *t*-test. N=4 independent experiments with >300
845 parasites each. Bar, 5 µm.

846 (*H*) Scanning electron micrographs of Hz purified from WT (3D7) and from DMSO or RAP-
847 treated *pv5-3xHA:loxP* schizonts. Bars, 500 nm.

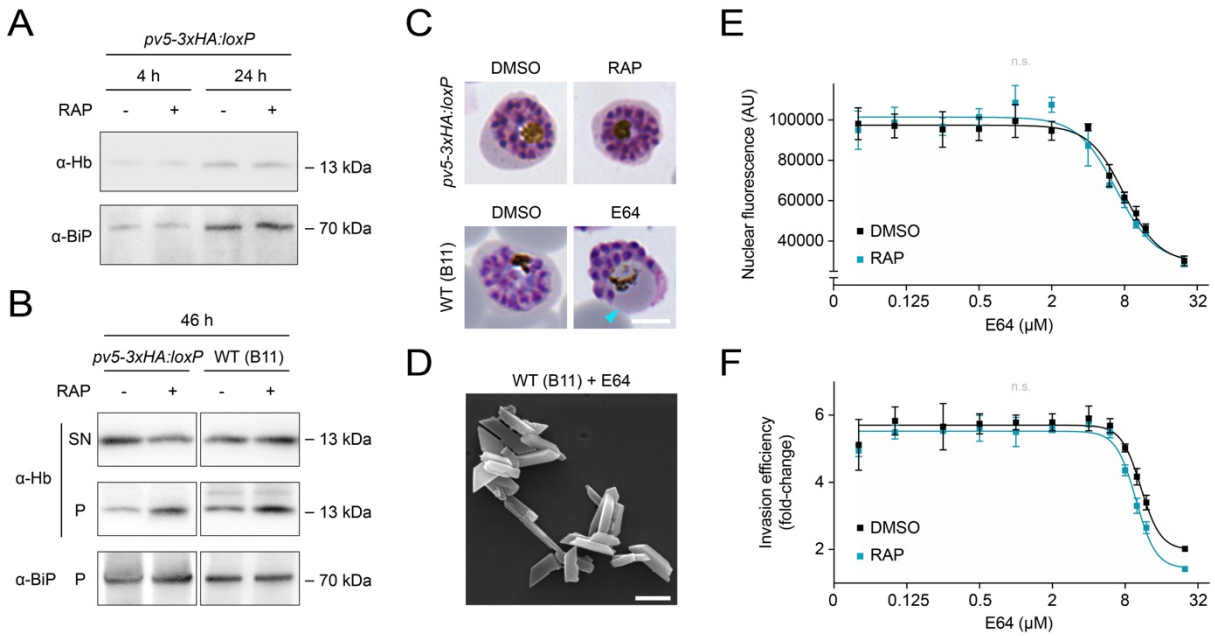

Fig. 5. *Pf*PV5 regulates haem sequestration independently from haemoglobin processing.

(*A, B*) Normal uptake and digestion of host cell haemoglobin by *Pf*PV5-deficient parasites. (*A*) Western blot analysis of induced and non-induced *pv5-3xHA:loxP* parasites released from their host cells by saponin lysis 4 and 24 hours after invasion. (*B*) 46 hours after invasion, induced and non-induced *pv5-3xHA:loxP* or WT (B11) schizonts were released by saponin treatment. Resultant supernatants (SN) and schizont pellets were isolated. Blots were probed with antibodies directed against human haemoglobin α (Hb) and *Pf*BiP. Note an increase in intraparasitic haemoglobin upon rapamycin treatment (RAP) in both *pv5-3xHA:loxP* and WT (B11) schizonts.

(*C*) *Pf*PV5-deficient schizonts exhibit no vacuolar bloating. Shown are *pv5-3xHA:loxP* parasites treated from the ring stage onward with dimethyl sulfoxide (DMSO) or RAP (top) and *Plasmodium falciparum* WT parasites treated from 24 hours post invasion onward with DMSO or 21.7 μM E64 (bottom). Cyan arrowhead, bloated food vacuole. Bar, 5 μm.

(*D*) Inhibition of haemoglobin catabolism does not result in abnormal Hz morphology. Shown is a scanning electron micrograph of Hz crystals isolated from the E64-treated *P. falciparum* WT parasites shown in *C*. Bar, 500 nm.

(*E, F*) *Pf*PV5-deficient parasites display unaltered sensitivity towards E64. DMSO and RAP-treated *pv5-3xHA:loxP* parasites were grown in various concentrations of E64 from the ring stage onward. (*E*) Nuclear SYBR Green fluorescence 44 hours after invasion. (*F*) Invasion efficiency under static conditions following a 36-hour incubation in the presence of E64 and subsequent inhibitor washout. Mean values +/- SD are shown. n.s., non-significant; fitting of IC_{50} values following non-linear regression, N=3.

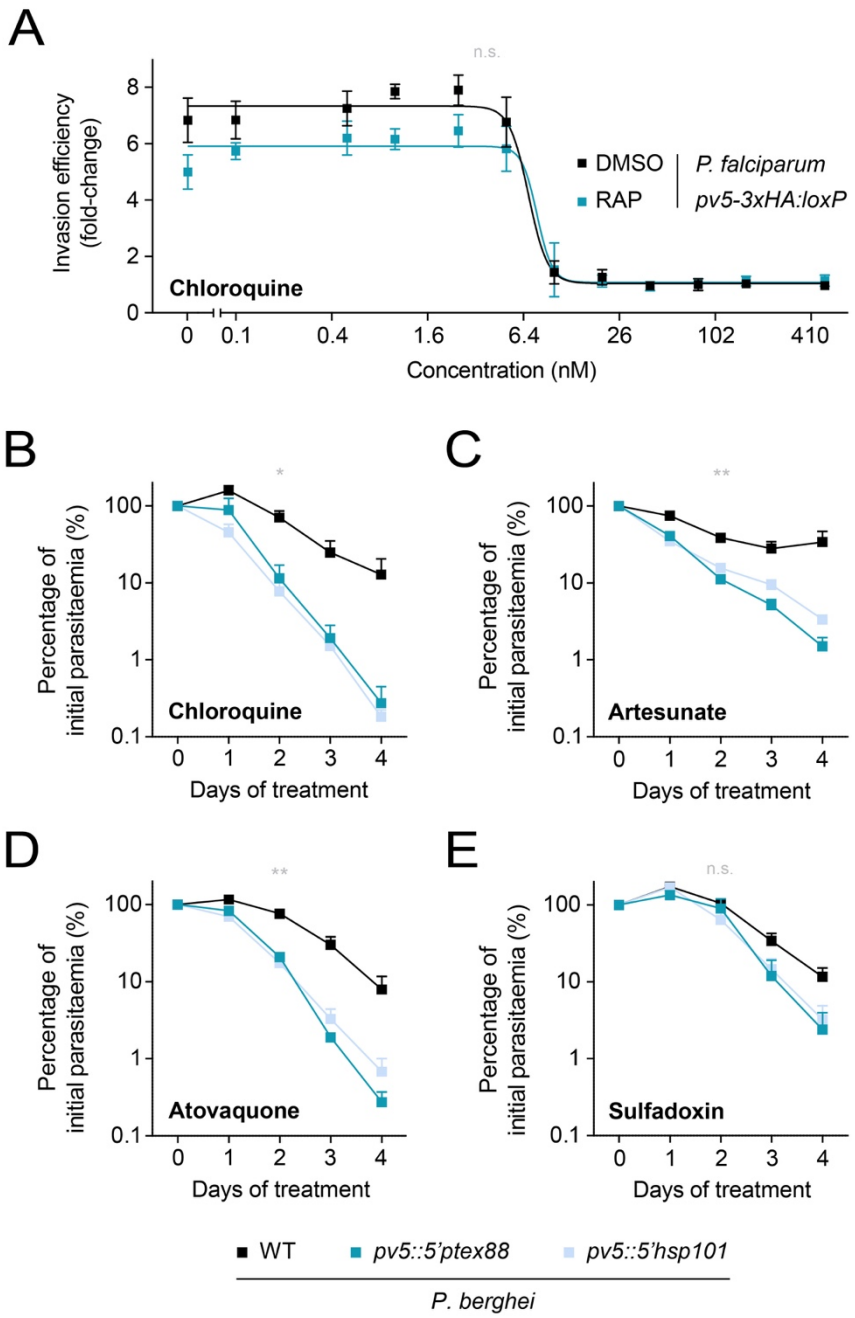

Fig. 6. Targeting PV5 function results in parasite hypersensitivity towards antimalarial drugs *in vivo*.

(*A*) PV5-deficient *P. falciparum* parasites retain normal sensitivity towards chloroquine. Shown is a dose-response analysis of DMSO- and RAP-treated *pv5-3xHA:loxP* parasites. Static ring stage cultures were treated with varying chloroquine concentrations and the transition into the following intraerythrocytic cycle was quantified. Depicted are mean values +/- SD. n.s., non-significant; fitting of IC_{50} values following non-linear regression, N=3.

(*B-E*) Enhanced drug susceptibility of the Pb*PV5* mutants *in vivo*. 5 x 10^6 mCherry-fluorescent *P. berghei* WT parasites were injected into SWISS mice together with 5 x 10^6 GFP-

881 fluorescent *pv5::5'ptex88* or *pv5::5'hsp101* parasites, respectively. From day three onward,
882 mice were treated with curative doses of (*A*) chloroquine (288 mg/l in drinking water, *ad*
883 *libitum*), (*B*) artesunate (50 mg/kg body weight, i.p.), (*C*) atovaquone (1.44 mg/kg body weight,
884 i.p.) or (*D*) sulfadoxin (1.4 g/l in drinking water, *ad libitum*) and the respective parasitaemias
885 were determined daily by flow cytometry of peripheral blood (50). Values are normalized to
886 the parasitaemias on day 0 of treatment. Shown are mean values +/- SEM. n.s., non-
887 significant; *, P<0.05; **, P<0.01; Two-way ANOVA. N=3 independent infections.

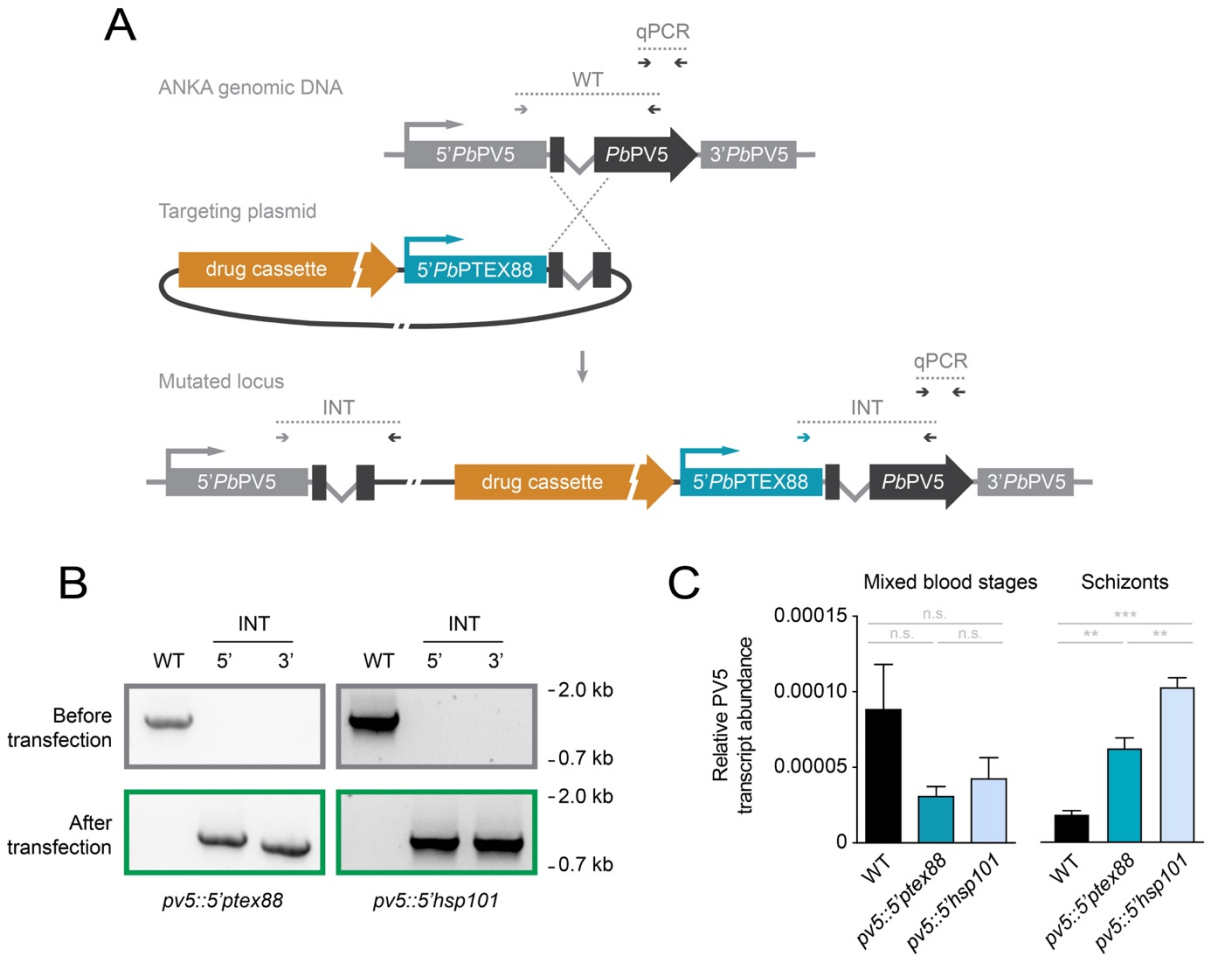

Fig. S1. Generation and validation of Pb*PV5* promoter swap mutants.

(*A*) Genetic strategy to exchange the endogenous promoter (light grey) of Pb*PV5* (dark grey) using single homologous recombination. The endogenous Pb*PV5* locus was targeted with an insertion plasmid containing the promoter sequence of Pb*PTEX88* (shown, blue) or Pb*HSP101* (not shown) fused to the amino-terminal sequence of Pb*PV5* as well as the drug-selectable hDHFR-yFcu cassette (orange). Successful insertion yields parasites expressing full length Pb*PV5* from a heterologous promoter and a non-functional amino-terminal fragment from the endogenous promoter, encoding the *Pb*PV5 signal peptide. Primer combinations for wild-type (WT) and integration-specific reactions (INT) as well as for quantitative real-time PCR (qPCR) are indicated by arrows and expected amplicons by dotted lines.

(*B*) Diagnostic PCR of the WT locus (top) and of the drug-selected and isolated Pb*PV5* mutants (bottom) using the primer combinations depicted in *A*.

(*C*) Dynamic changes in Pb*PV5* transcription upon promoter swap. Mixed blood stages and mature segmented schizonts were purified from mouse blood or from *in vitro* culture, respectively, and subjected to qPCR using primers targeting a carboxy-terminal portion of Pb*PV5*, as depicted in *A*. Pb*PV5* transcript abundance was normalized to *Pb*18S rRNA.

905 Shown are mean values +/- SEM. n.s., non-significant; **, P<0.01; ***, P<0.001; One-way
906 ANOVA and Tukey's multiple comparison test. N=6 for mixed blood stages and 3 for schizonts.

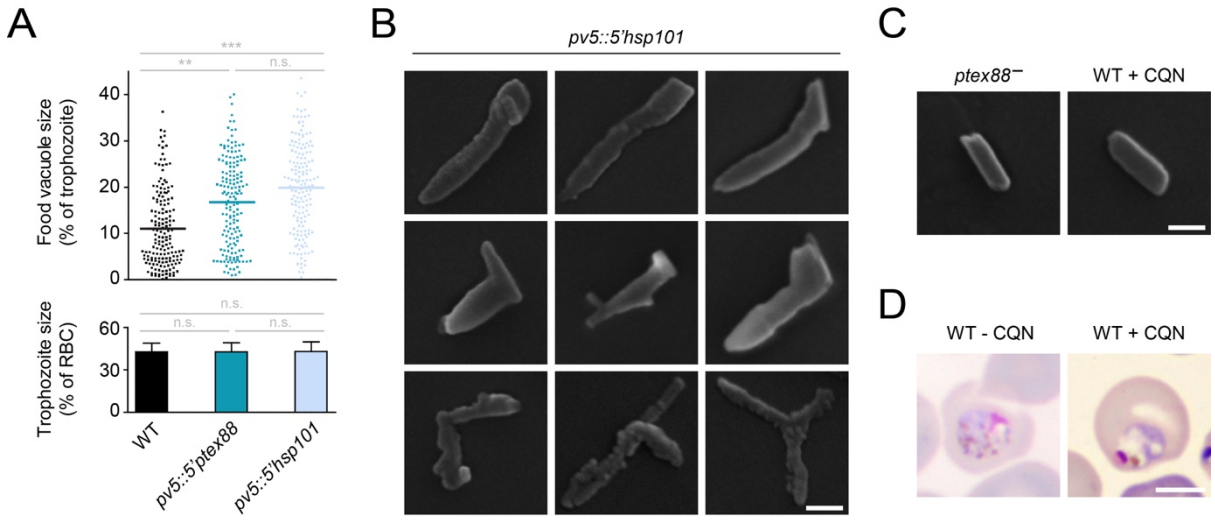

907

908 **Fig. S2.** Vacuolar dilation and defective haemozoin formation in the Pb*PV5* mutants.

909 (*A*) Quantification of vacuolar dilation. The translucent area observed in Giemsa-stained
910 trophozoites corresponding to the FV was measured microscopically and expressed as the
911 percentage of the entire trophozoite area (upper graph). Depicted are individual and mean
912 values (bars). Only trophozoites of identical size were analysed (lower graph). Shown are
913 mean values +/- SD. n.s., non-significant; **, P<0.01; ***, P<0.001; One-way ANOVA and
914 Tukey's multiple comparison test. N=165 trophozoites from 5 independent infections.

915 (*B*) A selection of Hz crystals generated by *pv5::5'hsp101* parasites as visualized by
916 scanning electron microscopy. Bar, 100 nm.

917 (*C*, *D*) Hz morphology is not affected by slow parasite growth or mortality. (*C*) Crystals
918 were extracted from slow-growing *PTEX88* knockout parasites (left) and from WT parasites
919 treated with curative doses of chloroquine (CQN, 288 mg/l in drinking water, *ad libitum*) (right)
920 and were visualized by scanning electron microscopy. Bar, 100 nm. (*D*) Morphology of
921 untreated (left) and CQN-treated WT parasites (right) as shown by Giemsa staining. Note the
922 pigment clumping and vesiculation in the dying parasite. Bar, 5 µm.

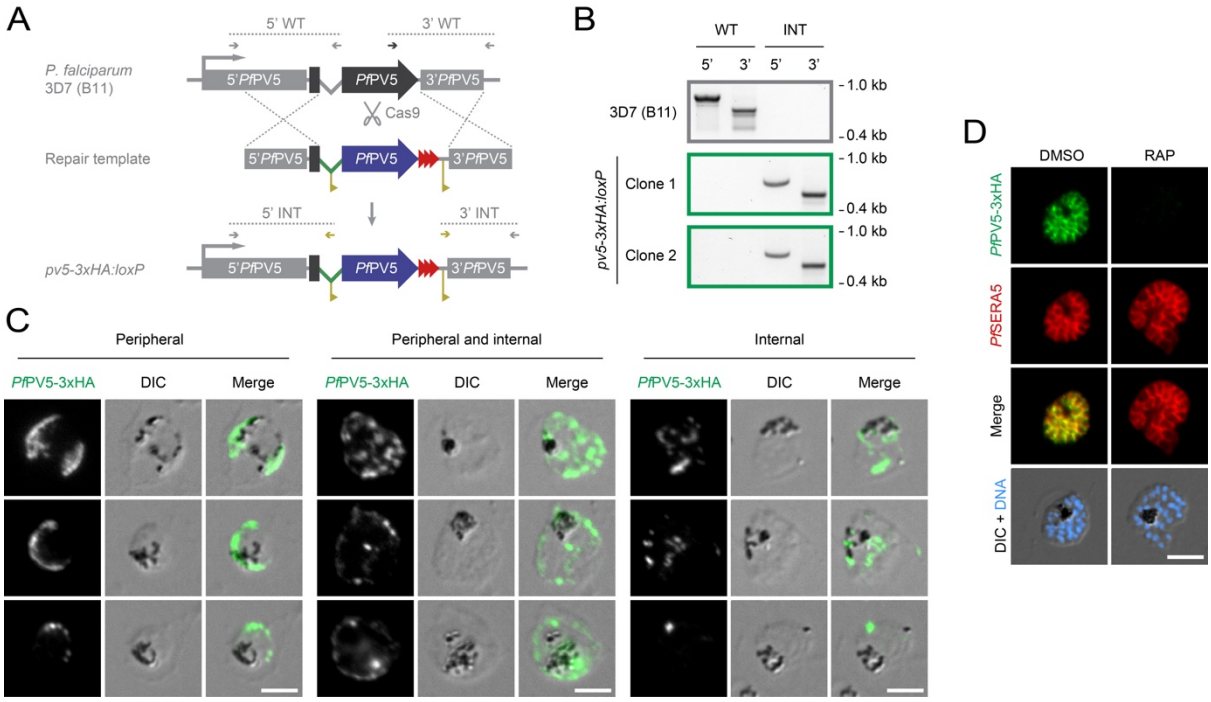

Fig. S3. Generation and validation of conditional Pf*PV5* knockout parasites.

(*A*) Genetic strategy for the generation of a conditional Pf*PV5* knockout line. The endogenous Pf*PV5* locus (dark grey) was targeted by Cas9-mediated double strand cleavage and repaired by homologous recombination with a synthetic template containing 5' and 3' homology arms (light grey), a 3xHA-tagged (red) re-codonised version of Pf*PV5* (blue) and *loxP* sequences (yellow) within the artificial intron (green) and behind the stop codon. Wild-type (WT) and integration-specific primer combinations (INT) are indicated by arrows and expected amplicons by dotted lines. Note that a second conditional knockout line was generated expressing *Pf*PV5 fused to mCherry (Fig. 1*E*).

(*B*) Diagnostic PCR of the recipient *P. falciparum* 3D7 (B11) line (top) and of two isolated *pv5-3xHA:loxP* clones (bottom) using the primer combinations depicted in *A*.

(*C*) Dual localization of 3xHA-tagged *Pf*PV5. Immunofluorescence analysis was performed using anti-HA primary antibodies. Depicted are exemplary *pv5-3xHA:loxP* trophozoites and young schizonts demonstrating localization of 3xHA-tagged *Pf*PV5 exclusively to the parasitophorous vacuole (PV, left), to the PV and internal parasite structures (centre) or to intraparasitic structures only (right). Shown are the signal of tagged *Pf*PV5 (green, left columns), differential interference contrast images (DIC, centre columns) and a merge (right columns).

(*D*) Loss of *Pf*PV5 protein. Immunofluorescence analysis of *pv5-3xHA:loxP* schizonts was performed with primary antibodies directed against HA and the PV protein *Pf*SERA5. Shown are the individual signals of 3xHA-tagged *Pf*PV5 (green, first row) and *Pf*SERA5 (red, second

945 row), a merge of both signals (third row) as well as a merge of DIC with Hoechst 33342 nuclear
946 stain (blue, fourth row) following treatment with DMSO (left) or RAP (right), respectively. Bars,
947 5 µm.

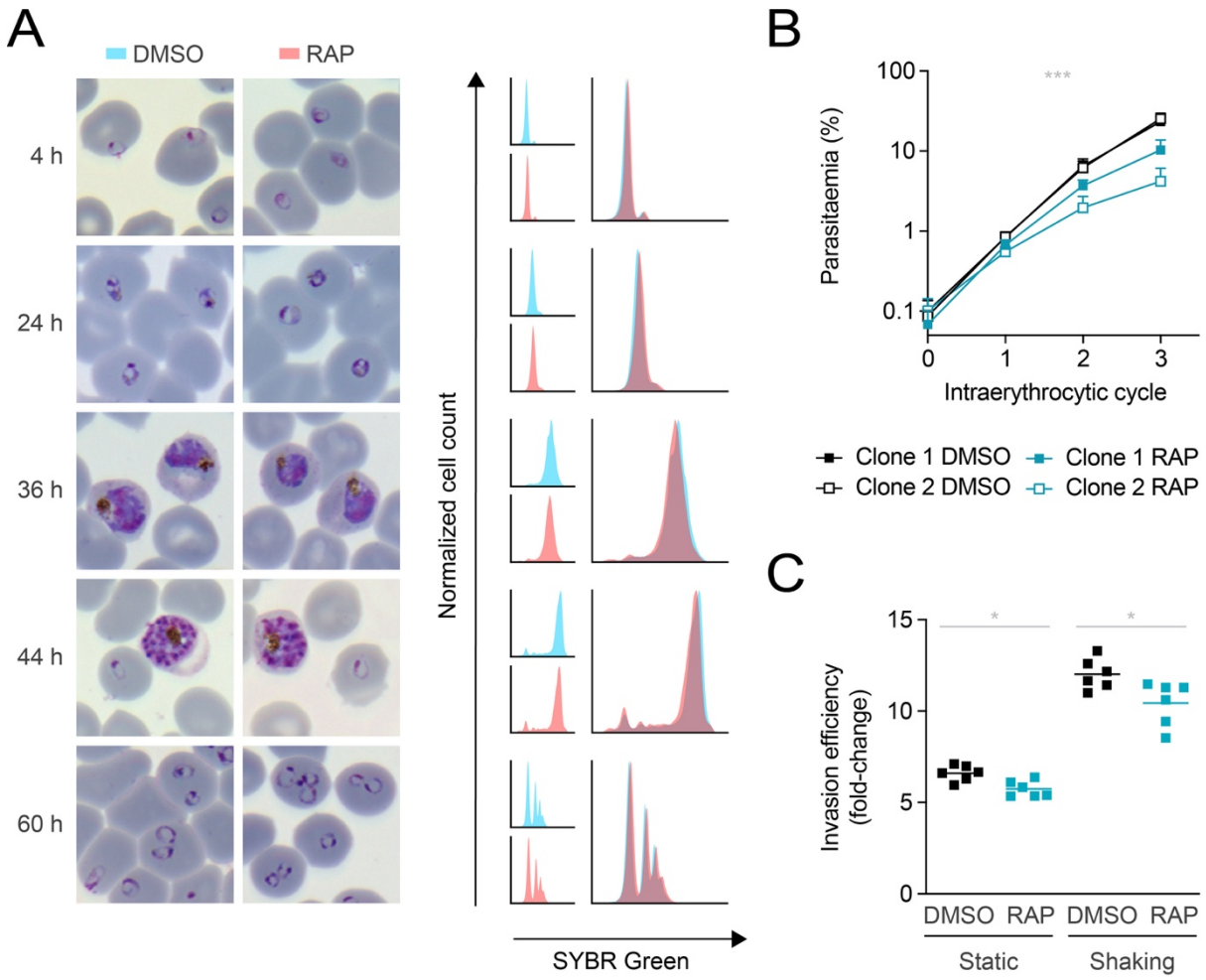

Fig. S4. Impaired fitness of *in vitro* cultivated *Plasmodium falciparum* in the absence of PV5.

(*A*) *Pf*PV5-deficient parasites mature normally *in vitro*. Tightly synchronized *pv5-3xHA:loxP* ring stages were treated with dimethyl sulfoxide (DMSO, blue) or rapamycin (RAP, red) and visualized by Giemsa staining 4, 24, 36, 44 and 60 hours later (left). In parallel, nuclear SYBR Green fluorescence was quantified by flow cytometry. Individual and merged histograms are depicted (right). Results are representative of two independent experiments.

(*B*) Asexual parasite proliferation is impaired upon loss of *Pf*PV5. Shown are growth curves of two independent *pv5-3xHA:loxP* clonal lines upon treatment with DMSO or RAP, respectively. Averaged parasite multiplication rates are 7.6 (DMSO) and 4.6 (RAP). Shown are mean values +/- SD. ***, P<0.001; Two-way ANOVA. N=6 independent infections.

(*C*) Impaired schizont to ring stage transition in the absence of *Pf*PV5. Schizonts from DMSO- and RAP-treated *pv5-3xHA:loxP* cultures were added to fresh erythrocytes and incubated under static or shaking conditions for 24 hours. Shown is the fold-change in parasitaemia, depicted as individual and mean values (bars). *, P<0.05; paired *t*-test. N=6 independent infections.

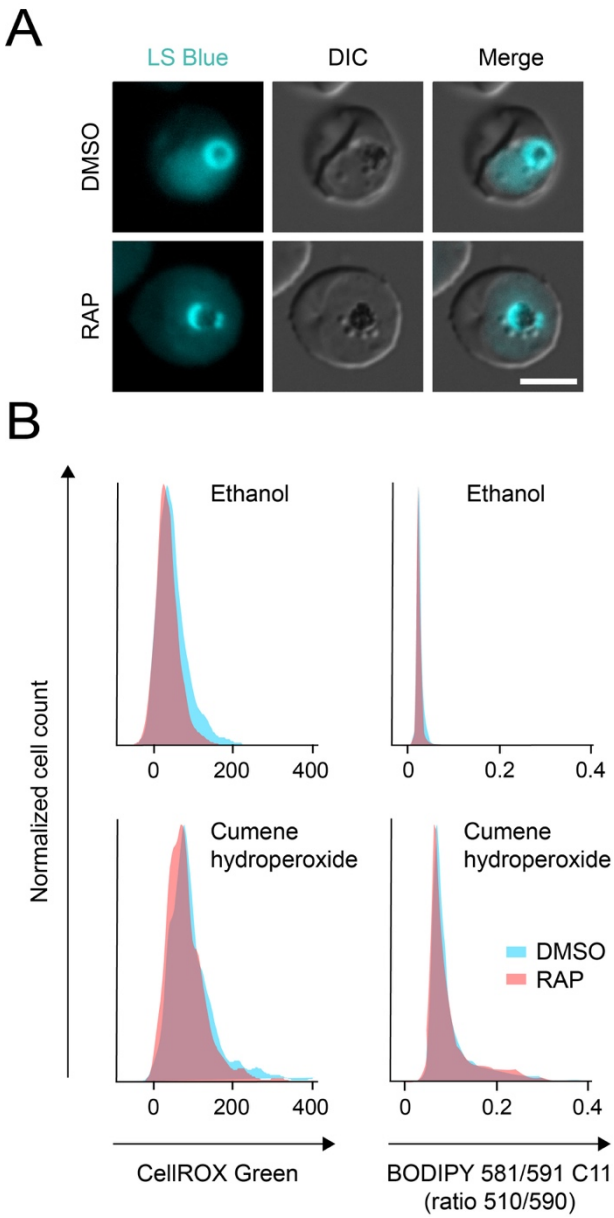

964

965 **Fig. S5.** Absence of *Pf*PV5 does not cause dissipation of the vacuolar pH gradient nor an
966 increase in oxidative stress.

967 (*A*) *Pf*PV5-deficient parasites maintain an intact and acidic FV. Synchronized *pv5-*
968 *3xHA:*loxP parasites were treated with dimethyl sulfoxide (DMSO) or rapamycin (RAP) from
969 the ring stage onward and were stained with Lysosensor Blue DND-167 (LS Blue) 36 hours
970 later. Shown are the LS Blue channel (cyan, left), differential interference contrast images
971 (DIC, centre) and a merge (right). Bar, 5 µm.

972 (*B*) No increased oxidative stress in the absence of *Pf*PV5. Synchronized *pv5-3xHA:loxP*
973 parasites were treated with DMSO (blue) or RAP (red) from the ring stage onward, stained
974 with the oxidative stress sensor CellROX Green (left) or with the ratiometric lipid peroxidation
975 dye BODIPY 581/591 C11 (right) 36 hours later and analysed by flow cytometry. In addition,

976 parasites had been treated with the oxidative stress-inducing agent cumene hydroperoxide
977 (bottom) or with ethanol as the solvent control (top). Shown are the histograms of CellROX
978 Green fluorescence intensity or of the 510/590 nm fluorescence ratio of BODIPY 581/591 C11.
979 Results are representative of two independent experiments.

980

981 **Movie S1.** Absence of *Pf*PV5 ablates haemozoin movement within the food vacuole of
982 *Plasmodium falciparum*.

983 Shown are differential interference contrast recordings of dimethyl sulfoxide (DMSO, left) and
984 rapamycin-treated (RAP, right) *pv5-3xHA:loxP* parasites 36 hours following invasion. The
985 video contains 120 frames shown at a 4x acceleration. Elapsed time is indicated in the upper
986 right corner. Bar, 5 µm.

987 **Table S1. Haemozoin crystal morphometry.**

	WT	***pv5-3xHA:loxP***		WT *vs.* DMSO	WT *vs.* RAP	DMSO *vs.* RAP
		DMSO	**RAP**			
Area (μm^2)	0.164 (±0.088)	0.107 (±0.052)	0.102 (±0.039)	***	***	n.s.
Aspect ratio	3.673 (±1.047)	2.781 (±1.061)	1.604 (±0.337)	***	***	***
Branching (%)	0	27.5	96.1			

988 n.s., non-significant; ***, P<0.001; One-way ANOVA and Tukey's multiple comparison test.
989 N>300 crystals.

990 **Table S2. Primer sequences.**

Primer Name	Primer Sequence (restriction sites)	WT (bp)[a]	INT (bp)[b]	EX (bp)[c]	Use[d]	Target	Reference
NT-PbPV5-F-BamHI	agttttggatccaaaatgaaattttatagcatttttgcaattg	707			TV	NT Pb*PV5*	This study
NT-PbPV5-R-SacII	agtattccgcggtttaaataacatttctgatttttttctcc				TV	NT Pb*PV5*	This study
5'-PbPTEX88-F-BamHI	aaatatggatccttttttgtgaaataagttgtttggtg	1,496			TV	5' Pb*PTEX88*	This study
5'-PbPTEX88-R-BamHI	atatatggatccaattttggggatttcaatctttttaag				TV	5' Pb*PTEX88*	This study
5'-PbHSP101-F-BamHI	ttaaaaggatccaaaaattatacaatgcgtgtggc	1,489			TV	5' Pb*HSP101*	This study
5'-PbHSP101-R-BamHI	ttttcaggatccatttatagtaaatatagatataattttatcttcattc				TV	5' Pb*HSP101*	This study
mCherry-F-AatII	aatttagacgtcatgaaggtgagcaagggcg	735			TV	*mCherry*	This study
mCherry-R-AatII	aatttagacgtccttgtacagctcgtccatg				TV	*mCherry*	This study
T7	taatacgactcactataggg		1,206		GT	T7	-
5'-PbPV5-F	gtgggtcgttatttgtatttttttaatattagg	1,440			GT	5' Pb*PV5*	This study
CT-PbPV5-R1	gatggatcataaccagcaacg				GT	CT Pb*PV5*	This study
5'-PbPTEX88-F	agtacgaagatataatttgaaaagcc		1,091		GT	5' Pb*PTEX88*	This study
5'-PbHSP101-F	tgcaactacattttattacgccc		1,177		GT	5' Pb*HSP101*	This study
CT-PbPV5-F	taaacccgttgatgaaaacactactgttg	261			qPCR	CT Pb*PV5*	This study
CT-PbPV5-R2	ggatcataaccagcaacgtaaagagc				qPCR	CT Pb*PV5*	This study
Pb18S-F	aagcattaaataaagcgaatacatccttac	134			qPCR	Pb*18S-rRNA*	(64)
Pb18S-R	ggagattggttttgacgtttatgtg				qPCR	Pb*18S-rRNA*	(64)
NT-PfPV5-F	attgattgttattatcatttccag	24			gRNA	NT Pf*PV5*	This study
NT-PfPV5-R1	aaacctggaaatgataataacaat				gRNA	NT Pf*PV5*	This study
5'-PfPV5-F	aatgcgggggaggagaaccc	836	730	2,006 / 1,260	GT	5' Pf*PV5*	This study
NT-PfPV5-R2	acaactccatcctatcaaaattaaag				GT	NT Pf*PV5*	This study
CT-PfPV5-F	catgatcattatgtctaaatatagaacc	670			GT	CT Pf*PV5*	This study
3'-PfPV5-R	atgtgaaaaaacttacaaactatataccc		561	2,006 / 1,260	GT	3' Pf*PV5*	This study
LoxP-F	taacttcgtatagcatacattatacg				GT	*loxP*	This study
LoxP-R	aacttcgtataatgtatgctatacg				GT	*loxP*	This study

991 [a] Sizes of Wild-type-specific PCR products or mCherry.

992 [b] Sizes of integration-specific PCR products.

993 [c] Sizes of excision-diagnostic PCR products (non-excised / excised).

994 [d] Primers used for construction of Transfection Vectors (TV), for GenoTyping (GT), quantitative real-time PCR
995 (qPCR), or for guide RNAs (gRNA). Used primer combinations are indicated in Figures 3*A* and Figures S1*A* and
996 S3*A*.